Rainer Pöttgen*, Oliver Janka and Bernard Chevalier

Cerium intermetallics CeTX – review III

DOI 10.1515/znb-2016-0013 Received January 13, 2016; accepted January 26, 2016

Abstract: The structure–property relationships of Ce*TX* intermetallics with structures other than the ZrNiAl and TiNiSi type are systematically reviewed. These Ce*TX* phases form with electron-poor and electron-rich transition metals (*T*) and *X* = Mg, Zn, Cd, Hg, Al, Ga, In, Tl, Si, Ge, Sn, Pb, P, As, Sb, and Bi. The review focusses on the crystal chemistry, the chemical bonding peculiarities, and the magnetic and transport properties. Furthermore ¹¹⁹Sn Mössbauer spectroscopic data, high-pressure studies, hydrogenation reactions and the formation of solid solutions are reviewed. This paper is the third of a series of four reviews on equiatomic intermetallic cerium compounds [Part I: R. Pöttgen, B. Chevalier, *Z. Naturforsch.* **2015**, *70b*, 289; Part II: R. Pöttgen, B. Chevalier, *Z. Naturforsch.* **2015**, *70b*, 695].

Keywords: cerium compounds; crystal structure; intermetallics; magnetic properties; structure–property relationship.

1 Introduction

The equiatomic intermetallic rare earth (RE) compounds RETX (T = transition metal; X = Mg, Zn, Cd, Hg, Al, Ga, In, Tl, Si, Ge, Sn, Pb, P, As, Sb, and Bi) have attracted the interest of solid state chemists and physicists for more than 40 years. Although these phases have a comparatively simple composition, they crystallize with more than 30 different structure types, a consequence of the difference in the covalent radii and the valence electron count [1–6]. The broad variations of T and T allow for distinct alterations of the physical properties. Systematic studies have particularly been carried out for the cerium, europium [7], and ytterbium [8] compounds which allow for

different valence states, e.g. Ce^{3+} vs. Ce^{4+} , Eu^{2+} vs. Eu^{3+} , and Yb^{2+} vs. Yb^{3+} . Thus, as a function of the T and X element it is possible to vary the magnetic ground states of the rare earth ions. Especially the cerium containing members have been deeply investigated in the context of strongly correlated electron systems [9–13].

The different valence states of cerium, e.g. diamagnetic Ce^{4+} with [Xe] configuration and paramagnetic Ce^{3+} with [Xe] $4f^1$ configuration, allow for a variety of physical properties in the field of Kondo compounds, antiferromagnetic and ferromagnetic ordering, valence fluctuations, heavy fermion compounds, superconductivity, or non-Fermi liquid systems. Almost a hundred CeTX phases have been studied over the last 40 years. Variation of the T and X elements changes the valence electron count as well as the crystal structure. Figure 1 gives an overview of the known CeTX phases, regrouping them with respect to their crystal structures.

The two largest groups concern the Ce*TX* phases with hexagonal ZrNiAl and orthorhombic TiNiSi type structure. The crystal chemistry and the physical properties of these phases have been systematically reviewed [14, 15]. The present review focusses on the remaining phases which adopt crystal structures of eight different structural families. Besides the crystal chemical details we emphasize the chemical bonding features and structure–property relationships including the formation of solid solutions and distinct property modifications that arise through hydrogenation reactions.

2 Synthesis conditions

The CeTX phases can all be prepared from the pure elements. The specific synthesis conditions, however, depend on the boiling temperatures of T and X. If all three elements have high boiling points or if the three boiling points are comparable, the CeTX phase is easily accessible via arc-melting [16–18]. Titanium or zirconium sponge or Ti/Zr alloys are usually pre-melted in the arc-melting chamber and act as oxygen and nitrogen getters. The product samples are normally melted two times on each side to ensure homogeneity. All high-melting CeTX phases are accessible through this technique, but also some of the plumbides [19] were obtained by arc-melting. Volatile

^{*}Corresponding author: Rainer Pöttgen, Institut für Anorganische und Analytische Chemie, Universität Münster, Corrensstrasse 30, 48149 Münster, Germany, e-mail: pottgen@uni-muenster.de Oliver Janka: Institut für Anorganische und Analytische Chemie, Universität Münster, Corrensstrasse 30, 48149 Münster, Germany Bernard Chevalier: Institut de Chimie de la Matière Condensée de Bordeaux, CNRS, Université Bordeaux, ICMCB, UPR 9048, F-33600 Pessac, France

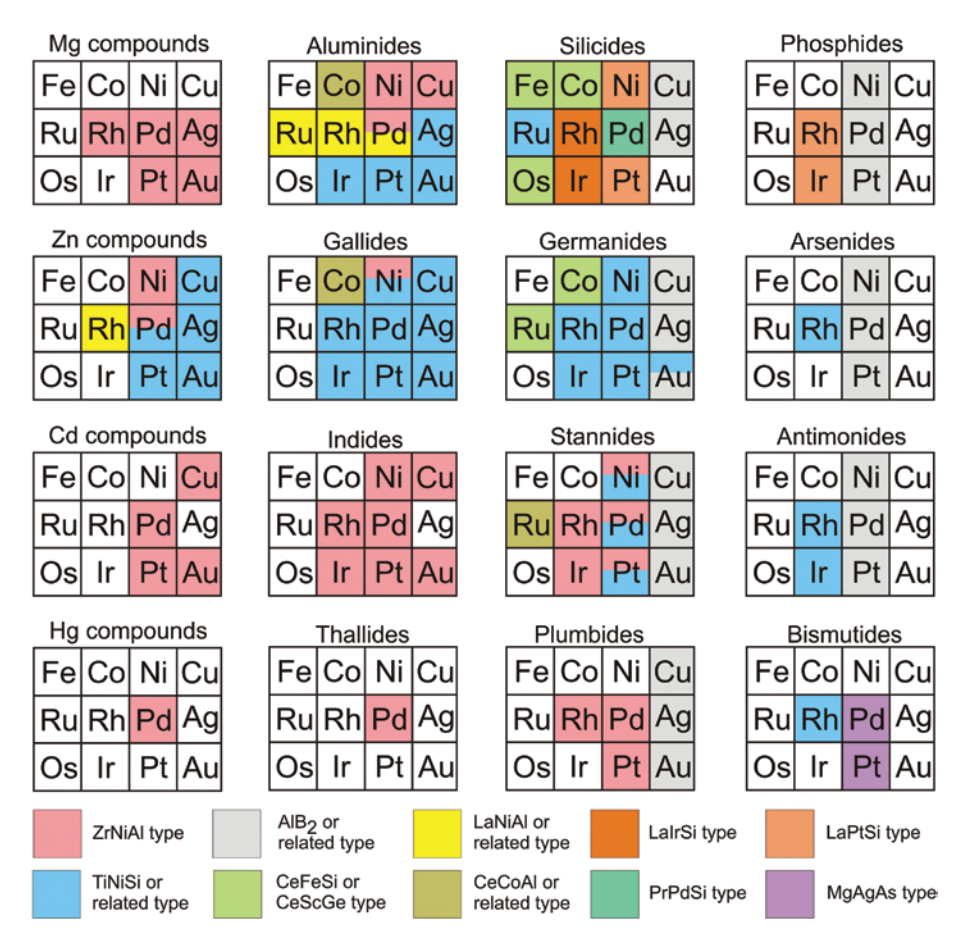


Fig. 1: Overview on the various CeTX phases color-coded based on their crystal structure. Some phases show dimorphism driven by temperature or pressure. The basic crystallographic data are listed in Table 1.

elements as antimony often lead to a weight loss during the repeated arc-melting process. In such cases an excess of 1.5-2.0 wt% antimony were used in the starting mixture in order to compensate the loss. A typical example is the synthesis of CeScSb [20, 21]. Usually the arc-melted products were additionally annealed in evacuated sealed silica tubes for further homogenization/equilibration. The specific annealing temperature depends on the sample. Here we refer to the original literature. In some cases the arc-melted product buttons were wrapped in tantalum foil as additional oxidation protection.

Also the classical ceramic route leads to Ce*TX* phases. CeRuSi, CeRuGe, and even CeOsSi (osmium has the extremely high melting temperature of 3320 K [22]) have been synthesized by this way [23]. The elements were weighed in the ideal atomic ratio and compacted to pellets in steel dies, followed by a heat treatment in sealed silica ampoules under 0.2 atm. argon pressure at 1173 K. This heat treatment was followed by induction-melting and a further annealing step at 1173 K for 2 weeks.

In the case of a T or X element with a comparatively low boiling temperature, arc-melting (an open-crucible

technique) leads to substantial weight losses through evaporation and the resulting samples do no longer have a well-defined composition. Compounds with zinc, mercury, or lead were prepared in sealed high-melting metal ampoules, usually made of niobium or tantalum [24–27]. These metal containers are then inductively heated in special sample chambers [28, 29]. Induction melting on a water-cooled tantalum support under flowing argon was finally used for the preparation of CeScSi and CeScGe samples [30].

The techniques described above mostly lead to polycrystalline samples. This might be sufficient for basic property studies; however, for structure determination and direction dependent property investigations single crystals are required. The crystals needed for single crystal X-ray diffractometer studies are often easily available since modern area detector diffractometers allow reliable structure refinements with crystal sizes in the lower micrometer scale. Sometimes such tiny crystals already form after the conventional heat treatment following the arc-melting. The crystals can be obtained by careful mechanical fragmentation of the buttons. Higher diffusion rates can be obtained by induction annealing of arc-melted samples in sealed silica ampoules in a watercooled sample chamber [31].

If the X element has a high liquidus range (low melting but high boiling temperature), metal flux [32] growth is a widely used technique for crystal growth. Often the flux medium can easily be dissolved after the reaction in diluted hydrochloric acid, while the product crystals resist. Well shaped crystals with a hexagonal tabular habit have for example been grown for CeCuSn from liquid tin [33].

Larger single crystals are required for direction dependent property studies. Such crystals have been grown on the mm or even cm scale. Larger crystalline parts of CePtSi are directly available by quick cooling from the melt [34].

The Czochralski technique is a standard method for the growth of larger crystals of intermetallics. Usually trior tetra-arc furnaces are used for the large sample quantities. The precursor samples were prepared in standard mono-arc furnaces. Large crystals of CeScSi, CeScGe [35], and CeRuSn [36, 37] were grown with this technique. CeAuGe crystals were grown with a floating zone technique [38]. Precise studies of the grown crystals showed significant macro-inhomogeneities along the length of the crystals, which is a bad prerequisite for property studies. A widely used method in the field of pnictides is the Bridgman technique. Crystals of CeTX (T = Pd, Pt, X =P, As, Sb) were grown with this method [39–42]. Tungsten crucibles were used as container material and in some cases, for the antimonides, a small excess of antimony was used.

At the end of this chapter we point to hydrogenation reactions of CeTX intermetallics. These syntheses did not focus on the search for new hydrogen storage materials but with respect to modifications of the physical properties [43–46]. The hydrogenation reactions start with the arc-melted precursor compounds which are first activated through heat treatment under vacuum, leading to better sorption kinetics (surface passivation often hampers the initial hydrogen uptake). The following hydrogenation reactions were carried out either at room temperature or at slightly elevated temperature under hydrogen pressures up to ca. 50 bars. The amount of absorbed hydrogen can be estimated from pressure changes in a calibrated volume. Homogeneity of the samples can be ensured by cycling the hydrides several times. The hydrogen uptake mostly leads to complete crumbling of the sample. For neutron powder diffraction experiments deuterium is used instead of hydrogen in order to reduce incoherent scattering.

3 Discussion

3.1 Crystal chemistry and chemical bonding

In this third review we summarize the crystal chemistry of the CeTX phases which crystallize with structures other than the ZrNiAl and TiNiSi types. The latter two series were reviewed in parts 1 and 2 of this series [14, 15]. A graphical overview based on the Periodic Table and with respect to the different structure types is given in Fig. 1. The basic crystallographic data of these phases are listed in Table 1. In the following subchapters we discuss the crystal chemistry of the CeTX phases in groups of related crystal structures.

3.1.1 CeTX phases with AlB, related structures

Most of the remaining phases discussed in the present review crystallize with ternary ordering variants of the AlB, type. Although more than 40 superstructures of the AlB, type are known today [1, 5, 47, 48], the phases discussed herein all keep hexagonal symmetry. A compact and concise way to systemize such structures relies on group-subgroup relations and is best monitored through a Bärnighausen tree [49-52]. A cutout of the complete Bärnighausen tree [47] is presented in Fig. 2 with an emphasis on the CeTX phases.

Keeping the Bärnighausen tree in mind it is readily evident, that T/X ordering is only possible for the YPtAs [53], ZrBeSi [54], NdPtSb [53]/LiGaGe [55], and SrPtSb [56] type structures. Nevertheless, many of the CeTX phases listed in Table 1 have been ascribed to the AlB, subcell structure or to the CaIn, type with a statistical distribution of the T and X atoms on the hexagons. In view of the largely differing chemical potentials of the T and X atoms, such random distributions are not the energetically stable ground state. There might be several reasons: (i) small homogeneity ranges $CeT_{1+x}X_{1+x}$ hamper long-range ordering and (ii) weak superstructure reflections have been overlooked. Especially in the case of similar scattering powers of the *T* and *X* atoms the superstructure reflections (which are the response of T/X ordering) are weak. Most likely all phases reported with one of the subcell structures are indeed ordered.

Before we discuss the structure types, we briefly comment on the symmetry reductions that lead to the different superstructures. In going from the AlB, subcell structure to the SrPtSb type (reported for CeNiAs [57]), the space group symmetry is reduced by a translationengleiche symmetry

Table 1: Lattice parameters of different Ce*TX* phases and some corresponding hydrides Ce*TX*H.

Compound	Structure type	Space group	<i>a</i> (pm)	<i>b</i> (pm)	<i>c</i> (pm)	$oldsymbol{eta}$ (deg)	V (nm³)	Magnetic behavior	References
Zinc compound			725.4(2)	20(((1)	4(22.4(1)		0.4754	DD.	[70]
CeRhZn	LaNiAl	Pnma	/35.1(2)	396.4(1)	1632.1(4)	90	0.4756	PP	[70]
Aluminides		=							
CeMnAl	MgCu ₂	Fd3m	802.4(1)		а	90	0.5166		[118, 119]
CeMnAlD _{1.94}	MgCu ₂	Fd3m	818.0(2)		а	90	0.5473		[118, 119]
CeMnAlD _{2.22}	MgCu ₂	Fd3m	821.0(2)		a	90	0.5534		[118, 119]
CeCoAl	own	C2/m	1109.8(7)		480.7(3)	104.61(5)	0.2777		[95]
CeRuAl	LaNiAl	Pnma -	721.8(2)	406.4(2)	1590.6(8)		0.4666		[99]
CeRuAl	LaNiAl	Pnma -		405.06(8)	1586.6(3)		0.4632		[71]
CeRhAl	LaNiAl	Pnma -		421.97(2)	1595.49(9)	90	0.4785		[71]
CeRhAl	LaNiAl	Pnma -		421.3	1593.9	90		$T_{\rm N} = 3.8 \; {\rm K}$	[115]
CeRhAl	LaNiAl	Pnma -		421.0(1)	1593.4(2)		0.4762		[116]
CeRhAl	LaNiAl	Pnma -	710.79(7)	422.64(5)	1593.14(17)	90	0.4786		[117]
a-CePdAl	own	Pmmn	426.07(5)	2887.58(10)	721.90(8)	90	0.8882	$T_{\rm N}=2.5~{\rm K}$	[72]
Gallides									
CeMnGa	$MgCu_2$	Fd3m	794.7	а	а	90	0.5019	P	[124]
CeMnGaH	MgCu ₂	Fd3m	810(1)	а	а	90	0.5314	n.i.	[125]
CeCoGa	CeCoAl	C2/m	1098.7(6)	436.7(5)	484.0(3)	102.99(4)	0.2263	n.i.	[95]
CeCoGa	CeCoAl	C2/m	1099.83(15)	435.20(6)	483.02(6)	103.260(7)	0.2251	$T_{\rm N} = 4.3 \; {\rm K}$	[96]
CeCoGaH ₃	AlB ₂	P6/mmm	430.1(4)	а	427.3(4)	90	0.0685		[125]
Indides	_								
CeZnIn	Caln,	P6 ₃ /mmc	478.7	а	763.1	90	0.1514	n i	[126]
CeZnIn	Caln,	$P6_3/mmc$	476.0		764.2	90	0.1500		[25]
CeCdIn	Caln ₂	$P6_3/mmc$	494.3		780.9	90	0.1652		[127]
	2	. 03/	15 1.5	4	, 00.5	, ,	0.1032		[/]
Silicides	I - Ch	11.1	(22.02(E)	_	4502.0(2)	00	0.2064	:	[405]
CeScSi	La ₂ Sb	I4/mmm	432.83(5)		1582.0(2)	90	0.2964		[185]
CeScSi	La ₂ Sb	I4/mmm	430.0(5)		1580(2)		0.2921		[186]
CeScSi	La ₂ Sb	14/mmm	431.5(1)		1586.4(2)	90		$T_{\rm N} = 26 {\rm K}$	[30]
CeScSiH	LaScSiH	14/mmm	425.4(3)		1675.1(5)			$T_{\rm N} = 3.0 \ {\rm K}$	[185]
CeMnSi	CeFeSi	P4/nmm	412.5(1)		728.5(2)	90		$T_{\rm N} = 240 {\rm K}$	[90]
CeMnSi	CeFeSi	P4/nmm	412.3(1)		729.0(1)	90	0.1239		[122]
CeMnSi	CeFeSi	P4/nmm	412.4		732.9	90	0.1264		[128]
CeFeSi	CeFeSi	P4/nmm	408.6(2)		678.8(3)	90	0.1133		[149]
CeFeSi	CeFeSi	P4/nmm	408.4(1)		678.3(2)		0.1131		[121]
CeFeSi	CeFeSi	P4/nmm	406.2(3)		675.2(5)	90	0.1114		[91]
CeFeSiH	ZrCuSiAs	P4/nmm	399.4(2)		781.0(4)	90	0.1246		[182]
CeCoSi	CeFeSi	P4/nmm	404.1(2)		699.0(2)	90		$T_{\rm N} = 8.8 \; {\rm K}$	[181]
CeCoSi	CeFeSi	P4/nmm	404.4(2)		699.3(2)		0.1144		[94]
CeCoSiH	ZrCuSiAs	P4/nmm	395.5(2)		786.1(3)		0.1230		[181]
CeNiSi	LaPtSi	I4 ₁ md	407.09(1)		1401.58(3)		0.2323		[75]
CeNiSi	LaPtSi	I4 ₁ md	407.0(2)		1403.0(5)	90	0.2324		[179]
$CeNiSiD_{\scriptscriptstyle{1.2}}$	LaPtSi	I4 ₁ md	404.11(1)		1423.53(2)	90	0.2325		[44, 75]
CeNiSiH _{0.8}	LaPtSi	I4 ₁ md	404.0(1)		1425.3(4)	90	0.2326		[179]
CeCuSi	Caln ₂	P6 ₃ /mmc	423.8		798.8	90		$T_{\rm c} = 14.9 \; {\rm K}$	[162]
CeCuSi	AlB ₂	P6/mmm	412.4		421.4	90	0.0621		[132]
CeCuSi	ZrBeSi	P6 ₃ /mmc	423.8(1)	а	803.5(3)	90	0.1250		[44]
CeCuSi	ZrBeSi	P6 ₃ /mmc	423.59(1)		798.08(1)	90		$T_{\rm c} = 15 \; {\rm K}$	[140]
CeCuSiH _{1.3}	ZrBeSi	P6 ₃ /mmc	419.4(1)		833.8(4)	90	0.1270		[44]
CeRuSi	CeFeSi	P4/nmm	419.8(2)	а	689.2(2)	90	0.1215	HF	[183]
CeRuSi	CeFeSi	P4/nmm	419.7(1)	а	689.4(4)	90		< 4.2 K	[23]
CeRuSiH	ZrCuSiAs	P4/nmm	417.98(5)	а	751.20(7)	90	0.1312	$T_{\rm N} = 7.5 \; {\rm K}$	[183]
CeRhSi	LaIrSi	P2 ₁ 3	623.1(1)	а	а	90	0.2419		[81]
CePdSi	PrPdSi	$P2_{1}^{1}/c$	1081.0(2)		789.1(1)	92.13(2)	0.4999	$T_{\rm c} = 7 {\rm K}$	[85]
CeAgSi	AlB ₂	P6/mmm	424.1(1)	а	420.3(1)		0.0655		[146]

Table 1 (continued)

Compound	Structure type	Space group	a (pm)	<i>b</i> (pm)	c (pm)	β (deg)	V (nm³)	Magnetic behavior	References
CePtSi	LaPtSi	I4 ₁ md	419.6(1)	а	1450.0(5)	90	0.2553	n.i.	[76]
CePtSi	LaPtSi	I4₁md	419.82(7)	а	1448.8(3)	90	0.2553	n.i.	[79, 147]
CePtSi	LaPtSi	I4₁md	420.2(1)	а	1448.4(4)	90	0.2557		[148]
CePtSi	LaPtSi	I4₁md	419.79(4)	а	1448.84(4)	90	0.2553	< 2 K	[145]
CeOsSi	CeFeSi	P4/nmm	415.9(2)		694.3(4)	90	0.1201		[23]
Germanides									
CeScGe	La ₂ Sb	I4/mmm	434.73(8)	а	1595.9(4)	90	0.3016	n.i.	[185]
CeScGe	La ₂ Sb	14/mmm	434.5(1)		1594.3(2)	90	0.3010		[188]
CeScGe	La ₂ Sb	14/mmm	431.4(2)		1591.3(8)	90	0.2962		[187]
CeScGe	La ₂ Sb	14/mmm	434.2(1)		1598.6(3)	90		$T_{\rm N} = 46 \; {\rm K}$	[30]
CeScGeH	LaŚcSiH	14/mmm	428.4(3)		1703.3(5)	90		$T_{\rm N}^{\rm N} = 3.1 {\rm K}$	[185]
lpha-CeTiGe	CeFeSi	P4/nmm	412.8(1)		790.8(1)	90	0.1348		[93]
lpha-CeTiGe	CeFeSi	P4/nmm	414.3(1)		796.0(4)	90	0.1367		[131]
α -CeTiGe	CeFeSi	P4/nmm	414.42		793.2	90	0.1362		[144]
α -CeTiGe	CeFeSi	P4/nmm	413.5(1)		792.1(1)	90	0.1354		[120]
β -CeTiGe	CeScGe	14/ <i>mmm</i>	414.95(2)		1590.85(10)	90	0.2739		[143]
CeMnGe	CeFeSi	P4/nmm	420.9(1)		738.7(1)	90	0.1309	n.i.	[122]
CeMnGe	CeFeSi	P4/nmm	422.32(2)		735.13(4)	90		$T_{\rm c} = 313 {\rm K}$	[182]
CeMnGeH _{1.1}	ZrCuSiAs	P4/nmm	414.08(2)		794.01(3)	90		$T_{\rm c} = 313 {\rm K}$	[182]
CeCoGe	CeFeSi	P4/nmm	417.0(2)		686.5(2)	90		$T_{\rm N} = 5.0 \rm K$	[139, 141]
CeCoGeH	ZrCuSiAs	P4/nmm	404.0(2)		773.5(4)	90	0.1162		[180]
CeCuGe	AlB ₂	P6/mmm	430.8(2)		396.6(2)	90	0.0637	n.i.	[137]
CeCuGe	AlB ₂	P6/mmm	429.6		398.8	90	0.0637		[137]
CeCuGe	-	P6/mmm	431.6(1)		396.7(1)	90	0.0640	n.i.	[130]
CeCuGe	AlB ₂					90	0.0040		
CeCuGe	ZrBeSi ZrBeSi	P6 ₃ /mmc P6 ₃ /mmc	429.11(2)		788.93(4) 795.19(1)	90			[189] [140]
			429.87(1)				0.1273	$T_{\rm c} = 10 \text{ K}$	
CeCuGe	ZrBeSi	P6 ₃ /mmc	430.2(1)		791.9(2)	90		n.i. n.i.	[44, 190]
CeCuGeH _{1.0}	ZrBeSi	P6 ₃ /mmc	424.4(1)		831.1(2)	90 90	0.1296		[44, 190]
CeCuGeD _x CeCuGe	own	P6 ₃ /mmc	422.90(2)		2481.5(2) 793.3	90			[189]
	Caln ₂	P6 ₃ /mmc	431.1					$T_{\rm c} = 10.2 {\rm K}$	[162]
CeZnGe	YPtAs	P6 ₃ /mmc	430.0(2)		1678.8(10)	90		$T_{\rm c} = 4.6 \; {\rm K}$	[133]
CeRuGe	CeFeSi	P4/nmm	427.5		687.1	90	0.1256		[184]
CeRuGe	CeFeSi	P4/nmm	419.5(2)		691.6(5)	90	0.1217		[138]
CeRuGe	CeFeSi	P4/nmm	427.5(1)		687.1(3)	90		< 4.2 K	[23]
CeRuGeH	ZrCuSiAs	P4/nmm	420.1		754.2	90		$T_{\rm N} = 4.0 \; {\rm K}$	[184]
CeAgGe	NdPtSb	P6 ₃ mc	454.42(2)		771.08(7)	90		$T_{\rm N} = 4.8 \; {\rm K}$	[142]
CeAgGe	Caln ₂	P6 ₃ /mmc	453.6(1)		774.6(3)	90	0.1380		[134]
CeAuGe	NdPtSb	P6 ₃ mc	446.03(7)		793.60(12)			$T_{\rm c} = 10.0 {\rm K}$	[136]
CeAuGe	NdPtSb	P6 ₃ mc	445.69(1)	а	791.05(1)	90	0.1361	$T_{\rm c} = 10.9 \; {\rm K}$	[135]
Stannides									
lpha-CeCuSn	NdPtSb	P6 ₃ mc	458.4(1)		785.8(2)			$T_{\rm c} = 8.6 \; {\rm K}$	[63]
eta-CeCuSn	ZrBeSi	P6 ₃ /mmc	455.8(2)		791.6(6)	90	0.1424		[63]
CeCuSn	Caln ₂	P6 ₃ /mmc	458.8		791.9	90	0.1444		[165]
CeCuSn	Caln ₂	P6 ₃ /mmc	458.3	а	786.5	90	0.1431	$T_{\rm N} = 8.6 \; {\rm K}$	[162]
CeCuSn	NdPtSb	P6₃mc	458.58(1)	а	784.85(2)	90	0.1429	n.i.	[44]
CeCuSn	NdPtSb	P6₃mc	458.537(1)	а	785.76(1)	90	0.1431	n.i.	[43]
CeCuSnD _{0.33}	own	P3m1	453.244(5)	а	406.60(1)	90	0.0723	n.i.	[43]
CeZnSn	YPtAs	P6 ₃ /mmc	456.7(3)	а	1673.8(5)	90	0.3023	$T_{\rm c} = 5.2 \; {\rm K}$	[59]
CeZnSn	YPtAs	P6 ₃ /mmc	456.5(1)	а	1670.8(2)	90	0.3015	n.i.	[161]
CeZnSn	YPtAs	P6 ₃ /mmc	456.9(1)	а	1676.6(6)	90	0.3031	n.i.	[160]
CeZnSnH _{1.5}	own	P6₃/mmc	449.34(9)	а	1731.3(4)	90		$T_{c} = 7.3 \text{ K}$	[157]
CeRuSn	own	C2/m	1156.1(4)	475.9(2)	1023.3(4)	102.89(3)	0.5488		[97]
CeRuSn	own	C2/m	1157.02(12)		1524.14(16)	103.511(2)	0.8132		[98]
CeAgSn	NdPtSb	P6 ₃ mc	477.7		774	90		$T_{\rm N} = 6.45 {\rm K}$	[123]
CeAgSn	NdPtSb	P6 ₃ mc	478.5(2)		774.9(8)	90	0.1537		[163]
_		5	- ()		,				1

Table 1 (continued)

Compound	Structure type	Space group	<i>a</i> (pm)	<i>b</i> (pm)	<i>c</i> (pm)	β (deg)	V (nm³)	Magnetic behavior	References
CeAuSn	NdPtSb	P6 ₃ mc	472.7(2)	а	771.6(3)	90	0.1493	n.i.	[61]
CeAuSn	NdPtSb	P6¸mc	473	а	771	90	0.1494	n.i.	[191]
CeAuSn	Caln ₂	P6¸/mmc	473.1(2)	а	771.2(3)	90	0.1495	$T_{\rm N} = 4.1 \; {\rm K}$	[164]
Plumbides									
CeMgPb	CeScSi	I4/mmm	455.7(1)	а	1642.6(2)	90	0.3412	n.i.	[27]
CeCuPb	NdPtSb	P6 ₃ mc	466.1(2)		778.1(3)	90	0.1464	$T_{\rm N} = 8.2 \; {\rm K}$	[26]
CeCuPb	NdPtSb	P6³mc	466.1	а	777.3	90		$T_{\rm N}^{\rm N} = 8.3 {\rm K}$	[25]
CeCuPb	NdPtSb	P6¸mc	465.81(4)	а	777.93(6)	90	0.1462		[156]
CeCuPb	Caln ₂	P6³/mmc	465.8	а	777.2	90	0.1460	n.i.	[126]
CeZnPb	YPtAs	P6³/mmc	463.7(2)	а	1669.6(6)	90	0.3109	$T_{\rm N} = 3.8 \; {\rm K}$	[155]
CeAgPb	NdPtSb	P6¸mc	484.8(2)	а	773.0(3)	90		$T_{N} = 7.4 \text{ K}$	[26]
CeAgPb	NdPtSb	P6³mc	484.39(3)	а	773.41(3)	90	0.1572		[19]
CeAgPb	NdPtSb	P6 ₃ mc	483.6(3)	а	767.0(5)	90	0.1553	n.i.	[154]
CeAuPb	NdPtSb	P6 ₃ mc	480.24(9)	а	772.9(2)	90	0.1544	$T_{\rm N} = 3.7 \; {\rm K}$	[26]
CeAuPb	NdPtSb	P6 ₃ mc	480.2	а	773.9	90	0.1545	n.i.	[153]
Phosphides									
CeNiP	YPtAs	P6 ₃ /mmc	399.4(1)	а	1608.5(7)	90	0.2222	n.i	[159]
CeRhP	LaPtSi	14 ₁ md	403.9		1435.3	90	0.2341	IV	[77]
CePdP	ZrBeSi	P6³,/mmc	424.8(1)		779.9(1)	90	0.1219		[60]
CePdP	ZrBeSi	P6³/mmc	425.1		781.0	90		$T_{c} = 5.2 \text{ K}$	[158]
CePtP	YPtAs	P6 ₃ /mmc	419.4		1602	90		$T_{c} = 3.1 \text{ K}$	[192, 193]
CeIrP	LaPtSi	14 ₁ md	404.8(2)		1428.8(11)	90	0.2341		[78]
Arsenides		1							
CeNiAs	SrPtSb	P 6 m2	413.4(1)	а	403.1(1)	90	0.0597	n i	[57]
CeNiAs	YPtAs	P6 ₃ /mmc	413.2(2)		1611.5(8)	90	0.2384		[151]
CePdAs	Caln ₂	P6 ₃ /mmc	437		780	90	0.1290		[127]
CePdAs	Caln,	P6 ₃ /mmc		a	779.7(1)	90	0.1289		[150]
CePdAs	ZrBeSi	P6 ₃ /mmc	437.6		781.2	90		$T_{c} = 6.2 \text{ K}$	[158]
CePtAs	NdPtSb	P6 ₃ mc	432		803	90		$T_{\rm N} = 1 \rm K$	[39]
		3	.52			, ,	0.1270	'N = 11	[27]
Antimonides CeScSb	CeScSi	1/1/2020	445.40(2)		1650 00(0)	00	0 2275	T _ 6 E V	[24]
		I4/mmm I4/mmm	, ,		1650.98(9)	90		$T_{\rm c} = 6.5 {\rm K}$	[21]
CeScSb CeNiSb	CeScSi ZrBeSi	•	446.6(1)		1654.1(5) 825.7(5)	90	0.3299		[20]
	ZrBeSi	P6 ₃ /mmc	439.3(3)			90	0.1380		[166]
CeNiSb _{0.9} CeNiSb	ZrBeSi	P6 ₃ /mmc P6 ₃ /mmc	439.4 442.7		823.8 830.2	90 90		$T_{c} = 4 \text{ K}$ $T_{c} = 4 \text{ K}$	[173]
CeNiSb	ZrBeSi	,	439.5(1)		825.8(4)	90			[173] [177]
CeNiSb	ZrBeSi	P6 ₃ /mmc			• •			$T_{\rm N} = 3.5 {\rm K}$ $T_{\rm N} = 3.5 {\rm K}$	[177]
CeNiSb	ZrBeSi	P6 ₃ /mmc P6 ₃ /mmc	437.6(3) 439.35(1)		819.2(5) 823.75(3)				[168]
CeNiSb	AlB ₂	P6/mmm	438.4		411.0		0.1377 0.0684		[167]
CeNiSb	AlB,	P6/mmm	438.4(2)		411.0(2)		0.0684		[174]
CePdSb	Caln,	P6 ₃ /mmc	459.4		791.3			$T_{\rm N} = 17 \rm K$	[169]
CePdSb	Caln,	$P6_3/mmc$	459.5		789.4		0.1443		[170]
CePdSb	Caln,	P6 ₃ /mmc	459.8(8)		789.5(9)			$T_{\rm c} = 16.5 \rm K$	[170]
CePdSb	NdPtSb	$P6_3mc$	459.8		791.4			$T_{\rm c} = 10.5 \rm K$ $T_{\rm c} = 17.5 \rm K$	[175]
CePtSb	NdPtSb	P6 ₃ mc	454.3		808.3			$T_{\rm c} = 4.7 \rm K$	[175]
CePtSb	Caln,	P6 ₃ /mmc	455.0		807.7		0.1448		[127]
CePtSb	NdPtSb	P6 ₃ mc	453.27		805.80	90		$T_{c} = 4.5 \text{ K}$	[172]
Bismuthides		. 030	.55.21	-	003.00	70	U.1-7J-7	· c 11.5 11	[=, 2]
CePdBi	ΜσΔσΛε	F 4 3m	602 A	a	a	00	0.3186	n i	[120]
CePdBi	MgAgAs MgAgAs	F43111 F43m	683.0 681.8(1)		a	90			[129]
CePdBi	MgAgAs MgAgAs	F43111 F43m	681.7(7)		a		0.3169		[86] [152]
CePtBi	MgAgAs MgAgAs	F43111 F43m	684		a a	90	0.3168	$T_{\rm c} = 2 \text{ K}$ $T_{\rm N} = 2.5 \text{ K}$	[152] [178]
	いいさいさんろ	1 サンロ1	004	u	u	70	0.5200	1 — Z.O N	11/0

IV, Intermediate valence; T_c , Curie temperature; T_N , Néel temperature; PP, Pauli paramagnet; HF, heavy fermion; SF, spin fluctuation; P, paramagnetic; n.i., not investigated. For samples that did not show magnetic ordering the lowest measuring temperature is given.

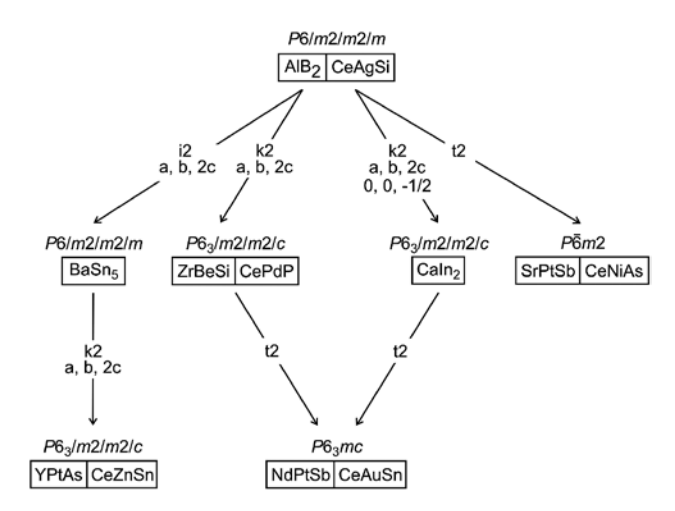


Fig. 2: Group-subgroup scheme in the Bärnighausen formalism [49-52] for CeTX phases that derive from the aristotype AlB₂. The indices for the translationengleiche (t), klassengleiche (k), and isomorphic (i) symmetry reductions, and the unit cell transformations are given.

reduction of index 2 (t2) from P6/mmm to $P\overline{6}m2$ (Fig. 2). In this case, the Ni/As ordering is only evident through changes in the subcell intensities. These intensity changes are weak, since nickel and arsenic differ only by five electrons.

The CaIn, structure [58] reported for many of the CeTX phases allows a puckering of the hexagons, however, only with random T/X distribution. The unit cell is doubled along the c axis through a klassengleiche symmetry reduction of index 2 (k2) along with a symmetry reduction from P6/mmm to P6₃/mmc (Fig. 2). This superstructure formation is expressed through the occurrence of additional reflections, so-called superstructure reflections. Ordering of *T* and *X* is then only possible through removal of the inversion center. This corresponds to a translationengleiche symmetry reduction of index 2 (t2) from P6₃/mmc to P6₃mc, leading to the NdPtSb type. Often these structures show twinning by inversion. All NdPtSb type CeTX phases show puckering of the $T_{\alpha}X_{\alpha}$ hexagons, and adjacent hexagons are rotated by 60°.

A similar ordering pattern, but with planar T_2X_2 hexagons occurs in the ZrBeSi type [54]. This structure derives from the AlB, subcell via a klassengleiche symmetry reduction of index 2 (k2) along with a doubling of the c lattice parameter (Fig. 2). The two symmetry reductions to the CaIn, and NdPtSb types lead to the same space group type, but different subcell mirror planes are lost. Puckering of the T_3X_3 hexagons occurs when the inversion center of the ZrBeSi type (translationengleiche symmetry reduction of index 2) is removed.

The largest unit cell of the hexagonal phases occurs for the YPtAs type compounds. This superstructure contains four AlB, subcells and requires two steps in symmetry reduction, an isomorphic step of index 2 to P6/mmm and a klassengleiche transition of index 2 to P6,/mmc. Both steps double the unit cell along the c axis.

Examples for the ordered phases are presented in Fig. 3 for CeZnSn [59], CePdP [60], CeAuSn [61], and CeNiAs [57]. The main crystal chemical motifs are ordered $T_{\alpha}X_{\alpha}$ hexagons perpendicular to the c axis with T-X distances close to the sums of the covalent radii, indicating substantial covalent T–X bonding within the networks. This was underlined by several electronic structure calculations.

The four different superstructures vary in the stacking sequence and the orientation of the T_xX_x hexagons. The simplest structure occurs for CeNiAs. The ordered Ni As, hexagons are planar and stacked in AA sequence. In CePdP every other planar Pd,P, hexagon is rotated by 60°, leading to AB stacking. CeAuSn can be considered as the puckered version of CePdP. Four ordered Zn₃Sn₃ hexagons are stacked in AA'BB' sequence in the structure of CeZnSn. Between the AA' and BB' layers one observes weak Zn-Zn and Sn-Sn inter-layer bonding. Stronger inter-layer bonding only occurs in CeAuSn and the other NdPtSb phases with puckered hexagons.

The cerium atoms in all these hexagonal CeTX phases are sandwiched by two $T_{x}X_{y}$ hexagons. The Ce-T and Ce-Xdistances are equal in the case of planar, but different in the case of puckered hexagons. Depending on the structure (YPtAs or NdPtSb type), the cerium atom are closer to T or X atoms (Fig. 3). In the NdPtSb type phases the closest contacts always occur for Ce−*T*. The degree of puckering depends on the size of the *T* and *X* atoms and some series of RETX phases show continuous transitions from two- to three-dimensional [TX] networks [62].

Finally we need to comment on the planar T_3X_3 hexagons. Many structure refinements have resulted in enhanced U_{33} parameters of the transition metal atoms, giving strong hint for the beginning of puckering. This phenomenon has been studied in detail for CeCuSn [63]. The low-temperature form crystallizes with the NdPtSb type with a puckering of the Cu₂Sn₂ hexagons, similar to CeAuSn. A quenched sample shows the ZrBeSi structure with large U_{33} parameters for the copper atoms. As emphasized in Fig. 4 one can rationalize this fact as a superposition of two differently tilted Cu₂Sn₂ hexagons since the diffraction data did only allow for a determination of the average structure.

The puckerings and distortions of the T_3X_3 hexagons can be influenced by external parameters. High-pressure studies of hexagonal CeAuGe (NdPtSb type) in diamond anvil cells revealed a transition to the orthorhombic TiNiSi type above 8.7 GPa [64]. This phase transition leads to a three-dimensional [AuGe] polyanionic network, while

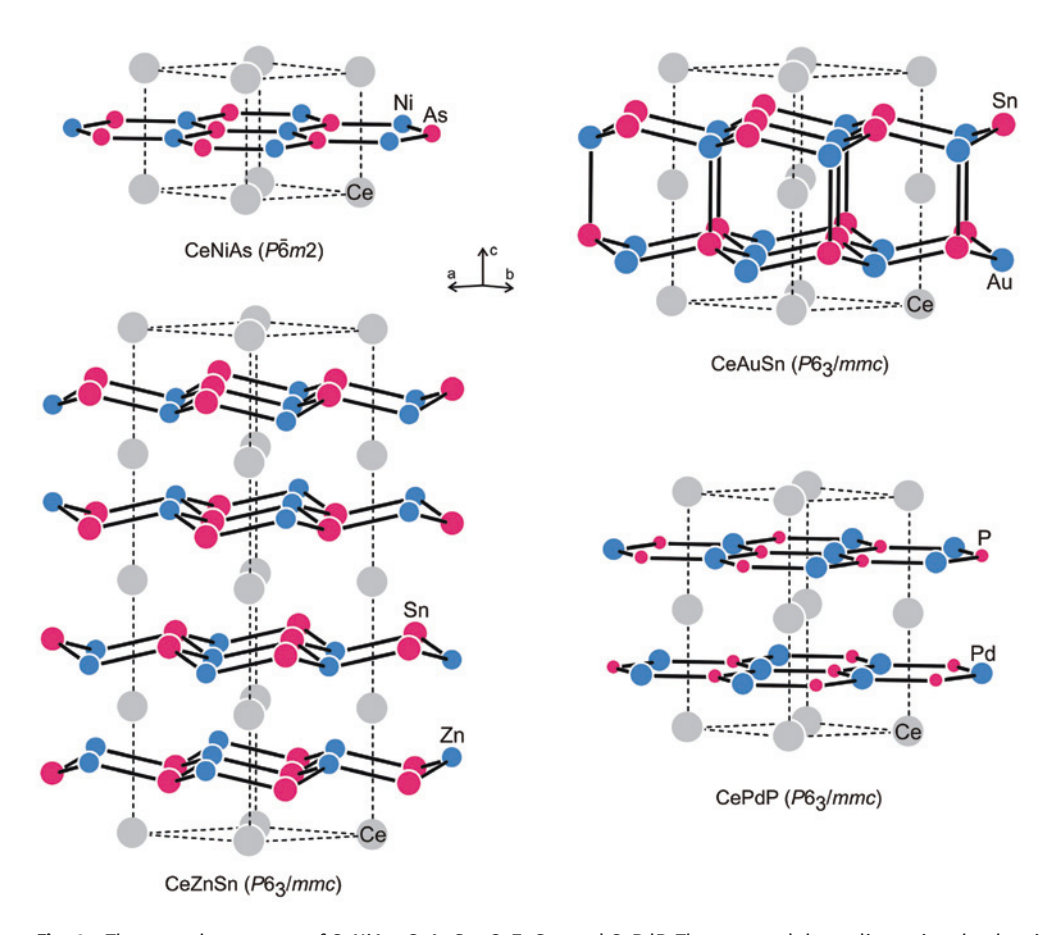


Fig. 3: The crystal structures of CeNiAs, CeAuSn, CeZnSn, and CePdP. The two- and three-dimensional polyanionic $[TX]^{\delta-}$ networks are emphasized.

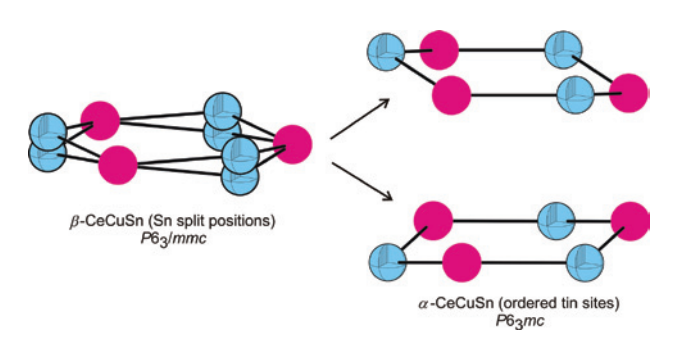


Fig. 4: Arrangement of the Cu_3Sn_3 hexagons in α - and β -CeCuSn. The copper and tin atoms are drawn as blue octands and magenta circles, respectively. β -CeCuSn shows disorder with a superposition of the ordered arrangements of α -CeCuSn. For details see text.

the puckered Au₃Ge₃ layers in the normal-pressure phase show two-dimensional character.

3.1.2 CeTX phases with LaNiAl and related structures

The LaNiAl structure type [65] is an intergrowth variant of TiNiSi [66] and ZrNiAl [67–69] type slabs. In the family of

CeTX intermetallics this structure type occurs for CeRhZn [70], CeRuAl, and CeRhAl [71]. As an example we present a projection of the CeRhZn structure in Fig. 5. The striking structural motifs are the rhodium centered trigonal prisms, similar to the TiNiSi and ZrNiAl phases [14, 15]. The CeRhZn structure contains two prism types, Rh@Ce and Rh@Ce₂Zn₂. These prisms are condensed via common edges within the ac plane and via common triangular faces along the b axis. Adjacent prismatic motifs are shifted by half the translation period of b. The rectangular faces of each prism are capped by a further atom, leading to coordination number 9, frequently observed in related intermetallic structures [1, 7]. The difference of this new arrangement of prisms as compared to the TiNiSi and ZrNiAl types is due to two crystallographically independent cerium sites in CeRhZn as compared to one site in the TiNiSi and ZrNiAl type CeTX phases.

An even more complicated condensation pattern of such prismatic units was found for the low-temperature modification LT-CePdAl [72]. As is evident from the projection presented in Fig. 5, now three prism types occur, Ce_c , Ce_aAl_a , and Al_c . The condensation pattern of

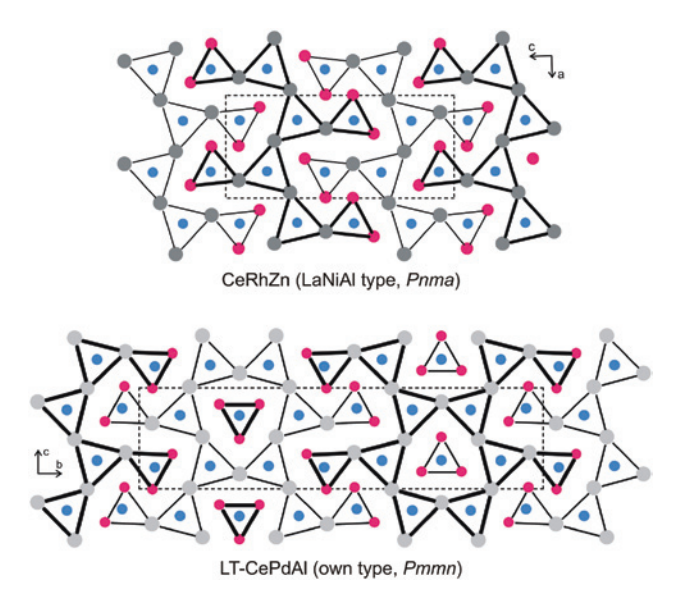


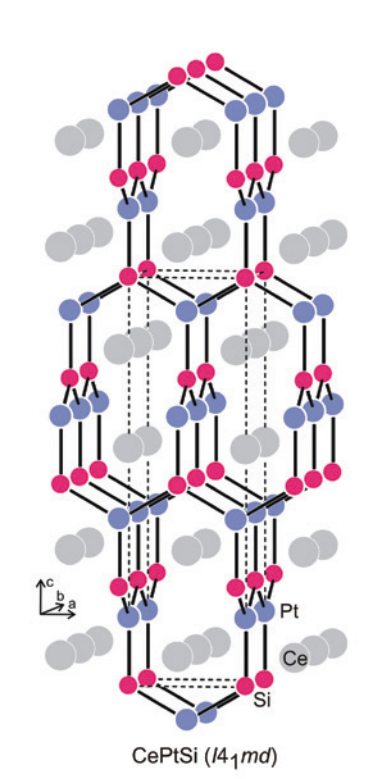
Fig. 5: Projection of the CeRhZn and LT-CePdAl structures along the short unit cell axis. Cerium, rhodium (palladium) and zinc (aluminum) atoms are drawn as light gray, blue, and magenta circles, respectively. The rhodium (palladium) centred trigonal prisms are emphasized. All atoms lie on mirror planes that are shifted by half a translation period, indicated by thin and thick lines.

the trigonal prisms is similar to that of CeRhZn, but the LT-CePdAl structure has larger ZrNiAl-related slabs. A detailed comparison of these structural variants was presented in the original work on CeRhZn [70] and LT-CePdAl [72] and in a recent summary of the solid solutions CeRu, Pd Al [73]. The lower space group symmetry in LT-CePdAl (as compared to CeRhZn) is expressed in four crystallographically independent cerium sites. Due to the different condensations of the trigonal prisms both CeRhZn and LT-CePdAl do not show the typical geometrical frustration which has intensively been discussed for the hexagonal CeTX phases [14].

Important parameters for the physical properties concern the Ce–Ce and Ce–*T* distances. In the hexagonal AlB, derived phases described in the previous subchapter and in CeRhZn and LT-CePdAl, the Ce-Ce distances are longer than the Hill limit of 340 pm for 4f electron localization [74]. This will be discussed further along with the magnetic data (vide infra).

3.1.3 CeTX phases with LaPtSi and LaIrSi type structures

The silicides CeNiSi [75] and CePtSi [76] as well as the phosphides CeRhP [77] and CeIrP [78] crystallize with the tetragonal LaPtSi type structure [79], a ternary ordered version of the α -ThSi, type [80]. The T/X ordering leads to a reduction of the space group symmetry from I4,/amd to 14,md through a translationengleiche reduction of index 2. The CePtSi structure is presented as an example in Fig. 6. The platinum and silicon atoms build up a threedimensional [PtSi] network with platinum and silicon in almost trigonal planar coordination. The Pt-Si distances of 242 pm are indicative of strong covalent Pt-Si bonding. The cerium atoms are placed within cavities of this polyanionic network. They have coordination number 12 by six platinum and six silicon atoms. The polyhedron consists



CelrSi (P2₁3)

Fig. 6: The crystal structures of CePtSi and CeIrSi. The three-dimensional [PtSi] and [IrSi] networks are emphasized.

of two parallel Pt_2Si_3 pentagons which are bridged by two further platinum atoms. This arrangement resembles the ZrNiAl type CeTX phases [14]. The two silicides and phosphides all have a valence electron count of 17 and can thus be considered as isoelectronic.

CeRhSi [81] and CeIrSi [82] adopt the cubic LaIrSi type [83] which is a ternary ordered version of SrSi₂ [84]. Similar to the tetragonal structure discussed above, the *T/X* ordering in CeRhSi and CeIrSi leads to a symmetry reduction from *P4*₁32 to *P2*₁3 (t2 step). The CeIrSi structure is presented as an example in Fig. 6. Each iridium atom has three silicon neighbors and vice versa in a slightly distorted trigonal planar coordination. This is similar to the [PtSi] polyanion discussed above. However, we observe a different connectivity pattern of these IrSi_{3/3} monomeric units. The Ir–Si distances of 229 pm again underline the strong covalent Ir–Si bonding. The cerium atoms have a slightly lower coordination number of 11 with 4 Ir and 7 Si neighbors. The valence electron count of CeRhSi and CeIrSi is 16.

3.1.4 CePdSi with PrPdSi type structure

The occurrence of a certain structure type for a Ce*TX* phase is not simply a function of the valence electron count or the size of the atoms. This is readily evident for the silicides Ce*TS*i (T = Ni, Pd, Pt). While the nickel and platinum compound crystallize with the tetragonal LaPtSi type (*vide supra*), CePdSi adopts the monoclinic PrPdSi structure [85]. The unit cell of CePdSi (space group $P2_1/c$) is quite complex at first sight (Fig. 7), however we find well known coordination motifs. Both crystallographically

independent palladium atoms in the three-dimensional [PdSi] polyanion have distorted trigonal-planar silicon coordination with Pd–Si distances ranging from 243 to 256 pm. This is indicative of substantial Pd–Si bonding. The coordination is similar to that in CeIrSi and CePtSi as discussed above, however, the condensation pattern of the TSi $_{3/3}$ monomeric units is different in the three compounds.

A peculiar feature of the CePdSi structure is the occurrence of Si–Si bonding (234 pm; single bond character) in the [PdSi] polyanion. This is different from all other Ce*TX* phases which exclusively show heteroatomic bonding. Both cerium sites have coordination number 12 with a different ratio of palladium to silicon: Ce1@Pd₇Si₅ and Ce2@Pd₅Si₇ A very detailed crystal chemical discussion of this unique structure type was published for the prototype PrPdSi [85].

3.1.5 CePdBi and CePtBi with MgAgAs type structure

The bismuthides CePdBi [86] and CePtBi [87] crystallize with the cubic MgAgAs structure [88], the so-called half-Heusler type [89]. As an example we present the unit cell of CePdBi in Fig. 8. Since all atoms reside on special positions, the interatomic distances of these phases can easily be calculated from the lattice parameters. The cerium and bismuth atoms in CePdBi build up a rocksalt-type substructure in which half of the tetrahedral voids are filled in an ordered manner by the palladium atoms. This leads to a hetero-cube-like coordination around each palladium atom, i.e. Pd@Bi₄Ce₄ with Pd-Bi and Pd-Ce distances of 295 pm, each.

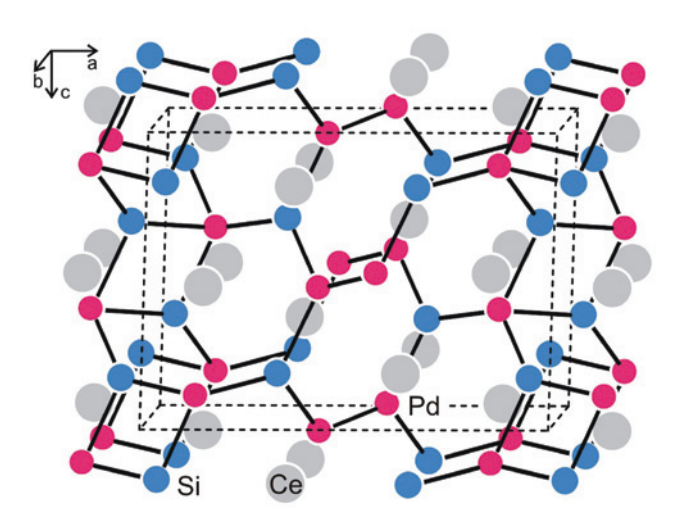


Fig. 7: The crystal structure of CePdSi, space group $P2_1/c$. The three-dimensional [PdSi] network is emphasized.

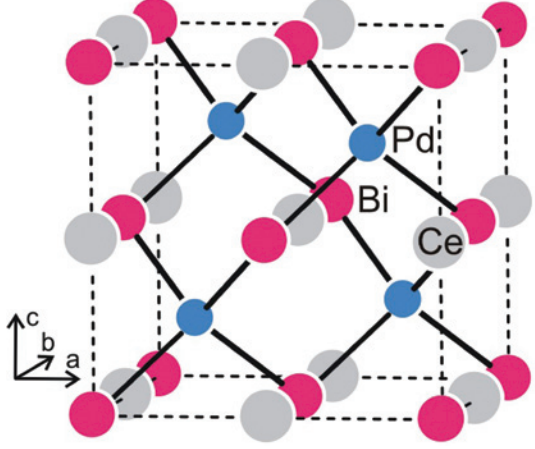
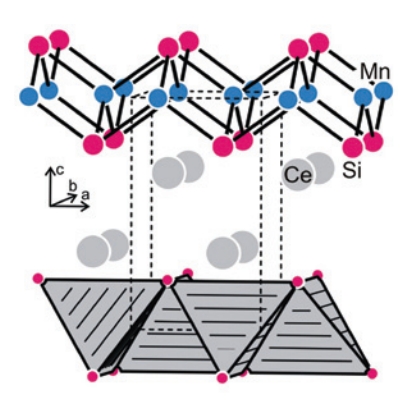


Fig. 8: The crystal structure of CePdBi (MgAgAs type structure). The tetrahedral bismuth coordination of the palladium atoms is emphasized.

3.1.6 CeTX phases with CeFeSi and CeScGe type structures

The next groups of CeTX intermetallics have tetragonal crystal structures. As an example we present CeMnSi [90] with CeFeSi type structure [91] and CeScGe with an ordered version of the La, Sb type [92] in Fig. 9. The manganese atoms in CeMnSi have tetrahedral silicon coordination with Mn-Si distances of 254 pm. These tetrahedra share common edges, leading to a dense layer perpendicular to the c axis. The MnSi_{ala} layers are separated by



CeMnSi (P4/nmm)

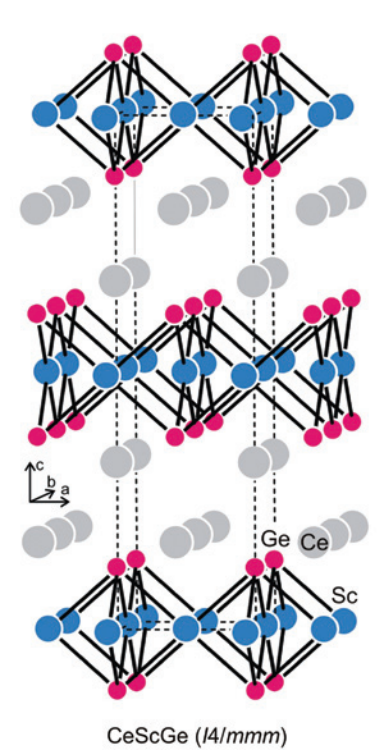


Fig. 9: The crystal structures of CeMnSi and CeScGe. The tetrahedral manganese-silicon coordination is emphasized in ball-andstick model and in polyhedral presentation. The planar $ScGe_{A/A}$ coordination is highlighted for CeScGe.

double layers of cerium atoms. The two cerium layers are shifted with respect to each other by 1/2 1/2 0 (a consequence of the n glide plane in space group P4/nmm). This way one obtains voids between tetrahedra of cerium atoms; a feature which is discussed later with respect to hydrogenation reactions.

The CeFeSi type occurs only for silicides and germanides in the family of CeTX intermetallics. The compound with the lowest valence electron count (VEC) is α -CeTiGe [93] (11 valence electrons) while CeCoSi [94] has a VEC of 16. Although this is quite a large range, α -CeTiGe can be considered as an exception, since most of the CeFeSi type phases have VECs between 14 and 16.

 α -CeTiGe shows a temperature induced transformation to α -CeTiGe with the CeScGe type (space group *I*4/*mmm*). The structure of the prototype is presented in Fig. 9. The scandium atoms form square grids at z = 0 and z = 1/2 with comparatively short Sc–Sc distances of 307 pm. They are coordinated by four germanium atoms in a rectangular planar fashion with Sc-Ge distances of 289 pm. The ScGe_{4/4} rectangles are condensed via common egdes and one obtains dense blocks perpendicular to the c axis, similar to CeMnSi discussed above. Again, every other layer is shifted by 1/2 1/2 0, since space group I4/mmm also contains an *n* glide plane. The stacking principle is then comparable to the P4/nmm phases. The [Sc₃Ge₃] layers are separated by double layers of cerium atoms which are also shifted with respect to each other and they also leave tetrahedral voids. The range of VECs is much smaller for the CeScGe phases; 10 for the pure rare earth phases and 11 for β -CeTiGe.

3.1.7 CeTX phases with CeCoAl related structures

The most complex structural behavior among the CeTX phases occurs for CeCoAl [95], CeCoGa [96], and the stannide CeRuSn [97, 98]. Our discussion starts with the subcell structure of the aluminide. A projection of the CeCoAl subcell structure along the monoclinic axis is presented in Fig. 10. The cobalt and aluminum atoms build up a complex three-dimensional network which leaves cavities for the cerium atoms. Around the inversion centers, symmetric Co₂Al₂ rhombs are the basic building motifs of the [CoAl] polyanionic network. These rhombs are connected via Al-Al contacts.

At ambient temperature CeRuSn [97] shows a doubling of the subcell c axis. This superstructure formation corresponds to an isomorphic transition of index 2 (i2) from C2/m to C2/m with a thinning of the symmetry elements. Half of the inversion centers are lost as a consequence of

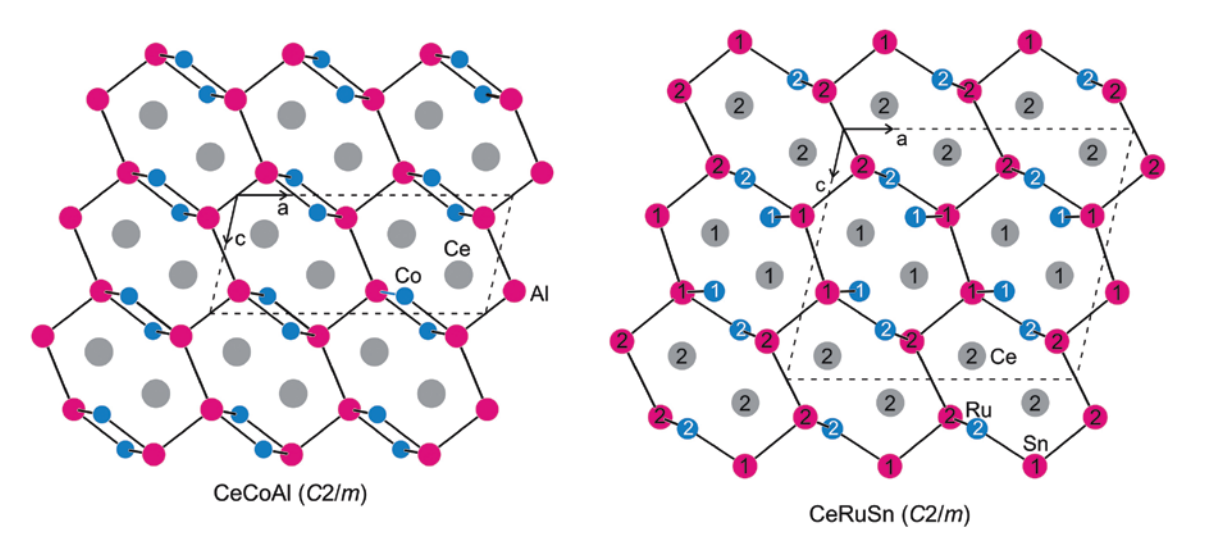


Fig. 10: Projection of the CeCoAl and CeRuSn structures along the monoclinic axis. The three-dimensional [CoAl] and [RuSn] networks are emphasized.

the symmetry reduction and the ruthenium atoms show a pronounced shift off the subcell positions. The consequences for the cerium coordination are shown in Fig. 11. The upper part of the drawing shows the average CeRuSn

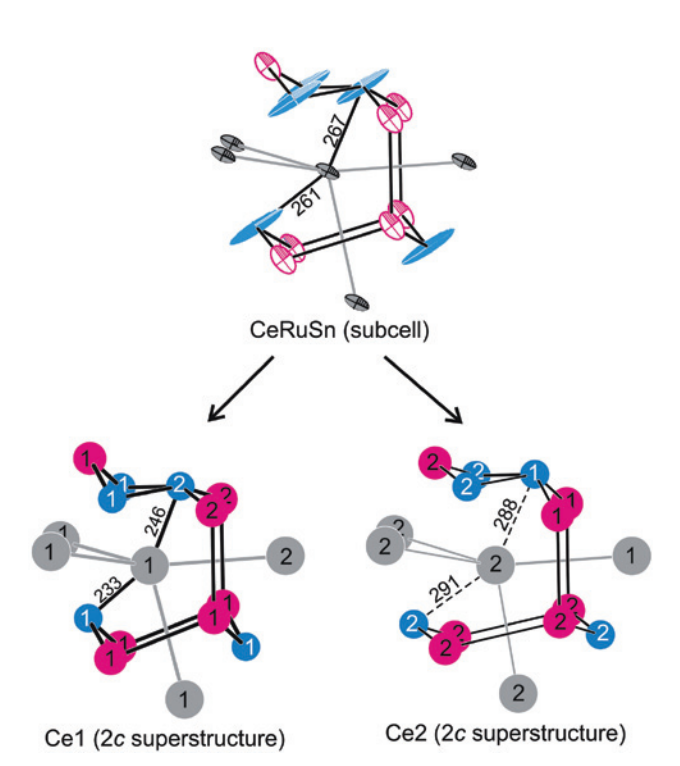


Fig. 11: Cerium coordination in the subcell and the 2*c* superstructure of CeRuSn. Cerium, ruthenium, and tin atoms are drawn as medium grey, blue, and magenta circles, respectively. Relevant Ce–Ru distances (in units of pm) and atom designations for the two crystallographically independent cerium sites of the superstructure are given.

structure, refined without the superstructure reflections. The ruthenium atoms show distinct anisotropic ellipsoids that are well resolved in the superstructure. The two crystallographically independent cerium sites in the superstructure are shown at the bottom of Fig. 11. The shifts of the ruthenium atoms lead to short Ce–Ru distances of 233 and 245 pm for Ce1 and an elongation to 288 and 289 pm for Ce2. This is a direct consequence of different cerium valencies: almost tetravalent Ce1 and trivalent Ce2, a kind of charge ordering in CeRuSn. This crystal chemical behavior with extremely short Ce–Ru distances seems unusual at first sight; however, meanwhile a whole series of ternary cerium ruthenium intermetallics has been published [99, 100] which all show the drastic shortening of the Ce–Ru contacts along with intermediate cerium valence.

Powders and single crystals (grown by the Czochralski technique) of CeRuSn have meanwhile been studied by a variety of techniques that all underline the intermediate cerium valence [101–109]. In going to lower temperature, CeRuSn shows a modulated structure which can be described within the superspace formalism in (3+1) dimensions. After a strong initial temperature dependence, the modulation vector approaches a value close to $\mathbf{q}=(0\ 0\ 0.35)$. The structural anomalies are in close relation with anomalies in the physical properties as discussed later.

Concerning the structurally related phases CeCoAl and CeCoGa, detailed studies of the phases of the CeCo-Al system [110–112], the enthalpies of formation [113], and the glass forming abilities [114] have been conducted. Recent reinvestigations of both structures revealed additional reflections, indicating superstructure formation. Heat capacity measurements of a CeCoAl sample [194]

showed a phase transition at 271 K and magnetic susceptibility measurements clearly substantiated the intermediate cerium valence. Satellite reflections occurred below 271 K giving rise to the superspace group $C2/m(\alpha 0\gamma)00$; $\alpha = 2/3$, $\gamma = 2/5$, with the q vector depending on the temperature. The driving force for the modulated superstructure is the formation of short Ce-Co distances. Similar results were obtained for CeCoGa [195]: superspace group $C2/m(\alpha 0\gamma)00$; $\alpha = 2/3$, $\gamma = 1/3$. Thermal analysis revealed a phase transition at 475 K. The two different superstructures were discussed on the basis of group-subgroup relations for reasonable approximants [195].

3.2 Magnetic and transport properties

The basic structural and electronic requirements that govern the magnetic ground states of the CeTX intermetallics have already been summarized in the previous reviews on the ZrNiAl and TiNiSi type materials [14, 15]. In the present chapter we discuss the magnetic and transport properties of the CeTX phases listed in Table 1. Most of these phases contain stable trivalent cerium with experimental magnetic moments close to the free-ion value of Ce³⁺. Many reports mainly deal with structural data and magnetic properties were only briefly studied. In cases where simple antiferromagnetic or ferromagnetic ordering was stated, the respective ordering temperatures are listed in Table 1. Those materials which were studied in greater detail are summarized in groups. CeTX phases that have been hydrogenated to a CeTXH, phase are discussed in chapter 3.4. Solid solutions based on CeTX phases are discussed separately in chapter 3.5.

3.2.1 CeMnSi, CeFeSi and CeMnGa

The CeTX silicide with the highest magnetic ordering temperature is CeMnSi [90, 128]. The manganese substructure shows antiferromagnetic ordering below $T_N = 240$ K. Neutron diffraction experiments revealed the arrangement of the magnetic moments. The magnetic structure shows an alternate stacking of antiferromagnetically coupling manganese layers, while the cerium layers are ferromagnetically coupled with opposite sign in every other layer. Variation of the refined magnetic moments indicates a Néel temperature of 175 K for the cerium magnetic substructure. The ordered moments on the manganese and cerium atoms were 2.71 and 0.78 $\mu_{\rm B}$, respectively. Conductivity measurements of CeMnSi have confirmed semiconducting behavior [128]. The sign of the Seebeck coefficient

changes from positive to negative around 220 K, indicating hole carriers below 220 K. The chemical bonding characteristics were derived from K and L band spectra using X-ray spectroscopy [196]. Substitution of manganese by iron completely changes the magnetic ground state. CeFeSi is a simple Pauli paramagnet [149].

CeMnGa [124, 197, 198] remains paramagnetic down to 4.2 K. The manganese and gallium atoms show random occupancy on the tetrahedral network of the MgCu, type structure, hampering long-range magnetic ordering. The magnetic moment in the paramagnetic range is 3.1 μ per formula unit along with a comparatively low paramagnetic Curie temperature of -144 K [198]. The specific resistivity of CeMnGa is > 100 $\mu\Omega$ cm over the whole temperature range. The large residual resistivity is another hint for atomic disorder within the CeMnGa sample.

3.2.2 CeTX phases with an electron-poor transition metal

The magnetic properties of CeScSi and CeScGe were determined on polycrystalline samples [30, 199] and Czochralski-grown single crystals [35, 200]. Both tetrelides order antiferromagnetically at 26 (CeScSi) and 46 K (CeScGe). These Néel temperatures (determined from susceptibility and specific heat measurements) are among the highest ones observed in the whole family of CeTX intermetallics [14, 15]. The stable antiferromagnetic ground states are supported by distinct metamagnetic steps at critical fields of 3.6 and 4.4 T for CeScSi and CeScGe, respectively. Single crystal data [35] showed directional differences for the metamagnetic steps which are more pronounced for the c axis. The antiferromagnetic ordering in both compounds is also evident as a weak kink in the resistivity measurements [199]. A discreapancy concerns parallel investigations which claim a ferromagnetic ground state for CeScGe based on LMTO electronic structure calculations [200]. The magnetic ordering temperature of CeScGe is susceptible to external pressure [201]. T_{N} decreases to ca. 15 K under a hydrostatic pressure of 60 kbar. This data was obtained from resistivity measurements.

The isotypic antimonide CeScSb [21] has a higher valence electron count. CeScSb orders ferromagnetically at $T_c \approx 9$ K, however, showing a broad peak in the specific heat data, most likely indicating some degree of disorder within the sample. Low-temperature neutron diffraction experiments have indicated additional magnetic intensity of the nuclear reflections. The cerium magnetic moments were determined to lie within the ab plane and the refined moment was 0.96 $\mu_{\scriptscriptstyle B}$ per cerium atom, substantially reduced when compared with the maximal value of 2.14 $\mu_{\mbox{\tiny R}}$

CeTiGe [131, 143, 144, 202, 203] is isoelectronic with CeScSb but exhibits two modifications, i.e. a CeScSi type high-temperature (space group I4/mmm) and a CeFeSi type low-temperature (space group P4/nmm) modification. This structural phase transition has a significant impact on the magnetic properties of the two modifications. The low-temperature modification shows stable trivalent cerium, but no magnetic ordering is evident down to 4.2 K [131]. Based on detailed resistivity and specific heat measurements, LT-CeTiGe has been classified as a non-magnetically ordered heavy-fermion system [144]. Seebeck coefficient measurements have revealed a maximum value around 60 µV K-1 at 17 K, and low-temperature magnetization studies showed a pronounced metamagnetic transition at a critical field of 12 T. Data was recorded up to an external field of 60 T [203]. Interestingly ordered moments close to 2 $\mu_{\scriptscriptstyle B}$ Ce atom⁻¹ were obtained at the highest field values, classifying CeTiGe as one of the remarkable CeTX materials. The high-temperature modification [143] shows no magnetic ordering down to 2 K and can be classified as a non-magnetic, strongly correlated electron system. Comparison of both CeTiGe modifications indicates a decrease of the crystal field hybridization parameter J_{cf} between the Ce 4f and the conduction electrons from LT- to HT-CeTiGe.

3.2.3 Intermediate cerium valence in CeRuSn, CeCoAl, and CeCoGa

CeRuSn is one of the outstanding materials in the family of CeTX phases. In the original study [97] a lock-in phase (2c CeCoAl superstructure) has been reported which contained two crystallographically independent cerium sites. Only one of these sites carries a magnetic moment and a remarkable hysteresis was observed below the phase transition temperature of 283 K. The hysteretic behavior has then been studied in more detail and it is also evident in the temperature dependence of the specific heat, the resistivity, and the Seebeck coefficient [102, 104]. The transitions also cause a strong shrinking along the *c* axis, as it was clearly proven from thermal expansion experiments on Czochralski-grown single crystals [36]. The trivalent cerium atoms in CeRuSn order antiferromagnetically below $T_N = 2.8$ K [103, 105]. The nuclear and the lowtemperature magnetic structure of CeRuSn was studied on the basis of powder and single-crystal neutron diffraction [103, 106]. The structure can be described by the superspace formalism in (3+1) dimensions. The nuclear propagation vector for this modulated structure is $q_{\text{nucl}} =$ (0 0 0.35). In the antiferromagnetically ordered regime a magnetic propagation vector of $q_{mag} = (0 \ 0 \ 0.175)$ has been determined. The magnetic structure refinement showed that the cerium magnetic moments are nearly collinear with the ac plane and modulated between values of 0.11 and 0.95 μ_n in *c* direction [106].

Parallel to the neutron diffraction studies, the subtle changes in the CeRuSn structure were investigated by the atomic pair distribution function as a local probe using high-energy synchrotron X-ray diffraction [107]. Additionally, the ratio of the two different cerium valences (Ce³⁺ vs. $Ce^{(4-\delta+)}$) was studied by XANES as a function of temperature [37, 108]. These two inequivalent cerium sites are also evident from polarized neutron diffraction studies. Below the transition temperature, a redistribution of the cerium spin densities became evident from the neutron diffraction data [109].

Many solid solutions based on the parent CeRuSn structure have thoroughly been studied with respect to cerium, ruthenium, and tin substitution. These results are summarized in a separate chapter at the end of this review.

Besides the very detailed studies of the physical properties of CeRuSn, only few data is known on the structurally closely related phases CeCoAl and CeCoGa. This is due to a more difficult sample preparation. Often tiny amounts of cobalt remain at the grain boundaries, hampering the property studies. Early studies of CeCoAl and CeCoGa [204–206] by thermal expansion, Seebeck coefficient, resistivity, and magnetic susceptibility measurements have already substantiated the deviation from a stable trivalent ground state for the cerium atoms. Especially magnetic susceptibility measurements showed a valence change with temperature, with almost tetravalent cerium at high temperature and a tendency towards intermediate cerium valence with decreasing temperature. Recent susceptibility data of CeCoGa have indicated antiferromagnetic ordering below $T_{N} = 4.3$ K. The presented band structure calculations, however, have suffered from the wrong structural model. The modulated structure with an adequate approximant was not known at that time.

3.2.4 CeTAl(T = Rh, Pd) and CeRhZn

CeRhZn, CeRhAl (both LaNiAl type) and LT-CePdAl (own type) are intergrowth structures with TiNiSi and ZrNiAl related slabs. These complex structures have two, respectively four crystallographically independent cerium sites. It is remarkable that CeRhZn [70] is a rare example of cerium intermetallics with multiple cerium sites where both kinds of cerium atoms are in an almost tetravalent state. Magnetic measurements have shown very weak susceptibility values and a very low moment of only 0.33 $\mu_{\scriptscriptstyle B}$ per cerium atom. This is in close agreement with electronic structure calculations, which showed almost empty 4*f* states above the Fermi level.

All cerium atoms in the low-temperature modification of CePdAl are trivalent. Susceptibility and specific heat data of LT-CePdAl show antiferromagnetic ordering at $T_N = 2.5$ K [72]. Due to the structural intergrowth, the strictly triangular building units are lost, leading to magnetic frustration in many of the hexagonal ZrNiAl type phases [14]. Resistivity measurements have confirmed classical Kondo lattice behavior.

Contradicting property studies were reported for CeRhAl. The early reports by Kumar and Malik claimed mixed valent behavior and no magnetic ordering for the cerium atoms [116, 207, 208]. Their samples showed substantial deviations from Curie-Weiss behavior over the whole temperature range. Both cerium valences were also evident from XANES spectra [208]. Reinvestigation of CeRhAl confirmed antiferromagnetic ordering of the cerium atoms at $T_{\rm N}$ 3.8 K [115]. The magnetic phase transition has also been substantiated through a well-defined lambda-type anomaly in specific heat measurements. Probable reasons for the discreapancy might be some degree of atomic disorder (Rh/Al mixing or formation of domains of a rhodium- and/or aluminum-rich solid solution) or the different annealing sequences used during sample preparation.

3.2.5 CePtSi and CeRuSi

CePtSi (space group I4,md) has thoroughly been studied on polycrystalline and single crystalline samples [34, 148, 209-219]. Susceptibility measurements showed stable trivalent cerium but no magnetic ordering down to the lowest available measurement temperatures. The remarkable feature derived from specific heat measurements is the extremely large gamma value of 700-800 mJ mol⁻¹ K⁻² [148, 209], classifying CePtSi as a heavy-fermion material. Independent measurements by different groups showed sample dependent properties. It was assumed that the sample composition and disorder effects might be the reason. Indeed, platinum-silicon mixing has been observed during a reinvestigation of the CePtSi structure [76]. Recent studies of the low-temperature properties down to the mK scale have confirmed that non-centrosymmetric CePtSi exhibits no quantum critical point [219]. Electrical resistivity measurements are in line with only very small crystal electric field splitting [34]. Temperature dependent Hall data point to the existence of a phase transition around 2.3 K [210], evident from an enhancement of the Hall effect. Resistivity measurements under pressures up to 15 kbar [213] have indicated a delicate interplay between Kondo lattice behavior and cerium mixed valence as a consequence of different interatomic distances. The crystal field parameters have been determined from inelastic neutron diffraction studies: 6.3 meV from the ground to the first excited state and 17.8 meV from the first to the second excited state [215].

Temperature dependent susceptibility studies of CeRuSi have shown trivalent cerium (2.56 $\mu_{\rm R}$ Ce atom⁻¹), while isotypic CeOsSi exhibits a substantially reduced experimental moment of only 2.03 μ_n Ce atom⁻¹ [23]. In addition, the smaller cell volume of the osmium phase is a strong hint towards intermediate cerium valence. This is in line with X-ray absorption spectra of the Ce L, edge [220], pointing towards partial delocalization of the cerium 4f electrons. The CeFeSi type structure of CeRuSi shows some anisotropy [183]. This has been studied in detail by ²⁹Si solid state NMR spectroscopy [221], where different shift components were observed for the ab and c directions.

3.2.6 The germanides Ce^TGe (T = Co, Cu, Ag, Au)

CeCoGe was first studied by Welter et al. [139]. Temperature dependent susceptibility data revealed Curie-Weiss paramagnetism and the experimental moment of 2.6 μ_D Ce atom-1 indicated a stable trivalent ground state. No magnetic ordering was reported in that study. Reinvestigation of CeCoGe by resistivity and magnetic susceptibility measurements pointed to antiferromagnetic ordering below $T_{\rm N} = 5.0$ K [141]. The magnetic structure was solved from neutron powder diffraction data and consists of ferromagnetic (001) planes that are antiferromagnetically stacked along c (+-+- sequence). A moment of 0.38 $\mu_{\rm R}$ per cerium atom has been refined from the 1.5 K diffraction data.

Ferromagnetic ordering at 10 K was determined for CeCuGe [222]. Saturation of the magnetization is already reached around an external field strength of 2 kOe (1 kOe = $7.96 \times 10^4 \,\mathrm{A}\;\mathrm{m}^{-1}$). The Curie point is also visible in the temperature dependence of the specific resistivity, however, the kink is weak. A decrease of the magnetic moment below 70 K in the paramagnetic range is attributed to crystalline electric field (CEF) effects. The corresponding parameters and the CEF scheme were deduced from inelastic neutron scattering data [140, 223]. CeCuGe shows a moderate Seebeck coefficient with a maximum value of ~10 µV K⁻¹ around 30 K. Isoelectronic CeAgGe orders antiferromagnetically at the much lower Néel temperature of $T_{\rm N}=4.8$ K [142]. The magnetic structure of CeAgGe shows a propagation vector ${\bf k}=[1/3~0~0]$. The cerium magnetic moments lie in the ab plane and a moment of 1.6 $\mu_{\rm B}$ per cerium atom has been determined [224].

CeAuGe orders ferromagnetically at $T_{\rm C}=10~{\rm K}$ [136, 225]. Similar to CeCuGe, also for the gold compound only a weak kink is observed in the temperature dependence of the specific resistivity. The ferromagnetic ordering was confirmed by neutron powder diffraction data at 1.7 K with a refined magnetic moment of 1.1 $\mu_{\rm B}$ per cerium atom, lying approximately along the *a* axis [224]. The CEF excitation (derived from the 4*f* contribution of the specific heat) amounts to $\Delta_{\rm CFF}/k_{\rm B}=240~{\rm K}$ [135].

3.2.7 The coinage metal stannides CeTSn (T = Cu, Ag, Au)

The magnetic properties of CeCuSn have repeatedly been studied for different poly- and single-crystalline (Czochralski method) samples [33, 63, 226-230]. Differences in the Néel temperature are due to structural disorder, e.g. a different degree of puckering of the Cu₃Sn₃ networks. Samples prepared at high temperatures or via quenching directly after arc-melting exhibit distinctly higher disorder than samples annealed for longer periods at lower temperature. This has been studied in detail by single crystal diffraction data [63]. The CeCuSn low-temperature modification shows a sharp increase of the magnetic susceptibility below 8.6 K, in agreement with antiferromagnetic ordering of the cerium magnetic moments [63]. Results of single-crystal neutron diffraction studies are in line with these observations and showed a magnetic wave vector of $k = (0.115 \ 0 \ 0)$ [33]. Susceptibility, resistivity, and specific heat studies on comparable Czochralski grown single crystals support this behavior [226]. The complex magnetic phase diagram was constructed from a large series of magnetization measurements [227]. Quenched CeCuSn samples show magnetic inhomogeneities [228, 229], a consequence of missing long-range order within the Cu₂Sn₃ networks. A detailed study of CeCuSn (along with CeAgSn and CeAuSn) by inelastic neutron scattering has led to precise values for the crystal field parameters [230].

CeAgSn orders antiferromagnetically at $T_{\rm N}=3.6~{\rm K}$ [231]. Neutron powder diffraction studies have revealed complete Ag-Sn ordering within the Ag₃Sn₃ hexagons. The propagation vector is ${\rm k}=(1/2~0~0)$ and a moment of 0.8 $\mu_{\rm B}$ per cerium atoms was derived from the diffraction data. Chemical bonding in CeAgSn was studied experimentally from X-ray photoemission spectroscopy [232]. The spectra were analyzed on the basis of the well-known

Gunnarsson–Schönhammer model, giving rise to absolute values for the energy levels. In addition, Fus et al. studied the total energies of CeAgSn for a disordered $CaIn_2$ type vs. an ordered LiGaGe type model, clearly underlining the fully ordered LiGaGe type.

The magnetic ground state of CeAuSn is finally antiferromagnetic at $T_{\rm N}=4.1$ K [123]. Experimental studies of the electronic structure of CeAuSn were performed by X-ray photoelectron spectroscopy [233]. The experimental and calculated valence band spectra showed good agreement.

3.2.8 Equiatomic plumbides CeTPb (T = Cu, Zn, Ag, Au)

So far, only few data is available for the Ce*T*Pb plumbides since they are all sensitive to moisture, hampering many property studies. The isotypic phases CeTPb with T = Cu, Ag, Au (all crystallize with the NdPtSb type) order antiferromagnetically below Néel temperatures of 8.2, 7.4, and 3.7 K, respectively [25, 26]. The magnetic phase transitions are clearly manifested by lambda-type anomalies in the temperature dependence of the specific heat. Resistivity data has only been reported for the copper phase. CeCuPb is a moderate metallic conductor. The plumbide CeZnPb [155] shows Curie-Weiss paramagnetism and the experimental magnetic moment is in good agreement with trivalent cerium. Antiferromagnetic ordering occurs below $T_{\rm N} = 3.8$ K. The stable antiferromagnetic ground state is supported by two pronounced, successive metamagnetic transitions at critical fields of approximately 1.1 and 7.0 kOe. Specific heat data give a hint for a spin reorientation at 2.6 K. Electronic structure calculations have confirmed the antiferromagnetic ordering and indicate that geometric frustration of the cerium magnetic moments is most likely the origin for the metamagnetic steps.

3.2.9 The antimonide CeNiSb

CeNiSb has repeatedly been studied with respect to its crystal structure and physical properties [166–168, 173, 176, 177, 234, 235]. Originally this antimonide was ascribed an AlB_2 structure, with a random occupancy of the boron network by nickel and antimony atoms. Subsequent studies indicated the ZrBeSi type structure with a complete ordering on Ni_3Sb_3 hexagons and rotation of every other layer by 60° . In this arrangement (space group $P6_3/mmc$) all Ni_3Sb_3 hexagons are planar. Since all X-ray diffraction studies on the diverse CeNiSb sample were carried out only on the basis of powder X-ray diffraction, it cannot be excluded that also a weak puckering of the

Ni,Sb, hexagons might occur. Keeping these structural constraints in mind, it is not surprising that slightly different properties have been reported. The local structure around the cerium atoms certainly depends on the thermal treatment of the samples. The structural disorder (planar vs puckered layers) is directly expressed in the strongly varying c lattice parameters of the different CeNiSb samples (Table 1).

Skolozdra and coworkers reported ferromagnetic ordering at $T_c = 7$ K [167] and classified CeNiSb as a Kondo system. The magnetic characterization was supported by resistivity and magnetoresistance measurements. The absence of magnetic ordering reported in a subsequent study is most likely due to a slightly different sample composition and/or structural disorder, preventing longrange magnetic ordering [166]. Kondo lattice behavior was confirmed by Menon and Malik, however, they reported a much lower Curie temperature of 4 K and also the possibility of off-stoichiometry for a sample CeNiSb_{oo} [173]. All available studies do not show a clear correlation of the Curie temperature with the lattice parameter c, clearly indicating that not only puckering but also differences in composition influence the coupling of the cerium magnetic moments.

The magnetic structure of CeNiSb was investigated on a larger, inductively melted sample using powder neutron diffraction [176]. A severe problem of larger powdered quantities of CeNiSb concerns surface oxidation. The powder diffraction patterns revealed small amounts of the sesquioxide Ce₂O₃. Evaluation of the neutron data indicated a modulated magnetic structure with a propagation vector $q = (0 \ 0 \ 0.25)$. Additional work using inelastic neutron scattering revealed the complete set of CEF parameters for CeNiSb [234].

The ferromagnetic ordering in CeNiSb is sensitive to substitution and external pressure [235]. A small degree of nickel-rhodium substitution leads to an increase of T_c from 4.6 K (CeNiSb sample) to 5.2 K for a starting composition CeNi_{0.9}Rh_{0.1}Sb. The resistivity behavior of CeNiSb was studied under external pressures up to about 20 kbar. Both the Curie and Kondo temperature significantly increase with pressure, a clear sign for an increase of the J_{cf} coupling, in agreement with the Doniach diagram [236–238].

3.2.10 Equiatomic pnictides CeTPn (T = Rh, Pd, Pt; Pn = P, As, Sb, Bi)

The physical properties of the remaining phases are discussed as a function of the pnictide component. CeRhP [77] crystallizes with the LaPtSi type with one crystallographic cerium site. Although it has a similar valence electron count as CePtSi (see chapter 3.2.5), the magnetic ground state is drastically different. CeRhP is a valence fluctuating compound with metallic character. The Kondo temperature was estimated to be 400-500 K.

CePdP contains stable trivalent cerium and orders ferromagnetically at 5.2 K [158]. Specific heat data revealed a moderate γ value of 69.2 mJ mol⁻¹ K⁻². Anisotropy in the CePdP structure was confirmed by the CEF parameters. CePtP has a lower Curie temperature of 3.1 K followed by a spin reorientation at $T_N = 1$ K [193]. A highly interesting point concerns the saturation magnetization. In the ferromagnetically ordered regime (2 K data) the magnetization is $2 \mu_{\rm p}$ per formula unit at 5 T and almost reaches the theoretical value of 2.14 $\mu_{\rm p}$. Full saturation is observed for the 0.45 K isotherm. The low-temperature antiferromagnetic state is supported by three successive metamagnetic transitions. Both phase transitions are clearly manifested in the temperature dependence of the specific heat. Magnetoresistance data and results of de Haas-van Alphen effect measurements point to cylindrical Fermi surfaces for CePtP and the isotypic arsenide CePtAs [192, 240]. These experimental results are in line with FLAPW band structure calculations. The binding energies determined through high-resolution resonance photoemission spectroscopy show remarkable differences for the bulk and the surface layers [42, 239].

Most studies on CePdAs were performed on single crystals which are accessible through the Bridgman technique [40, 241-245]. CePdAs is a 6.2 K ferromagnet [158, 241]. Resistivity measurements on CePdAs and the isotypic antimonide have shown a strong anisotropy, and both pnictides tend towards two-dimensional conductors [40]. Precise experimental studies on the electronic structures of CePdAs and CePdSb were performed through high-resolution resonance photoemission spectroscopy [242–245]. Small differences in the hybridization strength between CePdAs and CePdSb can be resolved in the spectra, and the experimental results are well reproduced by calculations using the single-impurity Anderson model [243]. In going to CePtAs [39, 246, 247] one observes a drastic reduction of the magnetic ordering temperature. CePtAs is a 1.0 K antiferromagnet and shows a pronounced metamagnetic step in the 0.54 K magnetization isotherm. Resistivity measurements showed the same anisotropy as for CePdAs and have substantiated the Kondo-type character.

The most remarkable and deeply studied pnictide is CePdSb [41, 169, 171, 175, 248–260] due to its high Curie temperature of 17 K. Magnetization measurements revealed the typical reduced magnetic moment in the ordered state, a consequence of anisotropy and CEF splitting. The onset of ferromagnetic ordering is also evident as a strong drop in the temperature dependence of the specific resistivity [248], due to a reduction of spin-disorder scattering. This is similar to the temperature dependence of the Seebeck coefficient where a steeper slope was observed below $T_{\rm c}$ [258]. The maximum Seebeck value of ca. 70 mV K⁻¹ occurs at room temperature [250, 258]. Under hydrostatic pressure one observes a significant increase of the Curie temperature with a maximum value of 31 K at 10 GPa [251, 257].

The thermal expansion of CePdSb single crystals (Bridgman crystal growth) shows a strong anisotropy [253, 256]. The expansion coefficient is one order of magnitude larger in the magnetically hard c direction as compared to a and b. This anisotropy is independently evident from a detailed evaluation of the specific heat data [249] which are not compatible with a simple isotropic exchange model but point to differences in inter- and intra-chain exchange parameters J. A parallel study of CePdSb via ¹²¹Sb(¹²³Sb) NMR as a function of pressure has underlined the pressure-dependent susceptibility data [254]. A summary of the CePdSb properties and a comparison with related CeTX phases under consideration of the valence electron count has been published by Ślebarski [259].

CePtSb has a lower Curie temperature of $T_{\rm c}=4.7~{\rm K}$ [41, 175, 260–262]. The experimental data were also measured on single crystals and the anisotropy was comparable to that of CePdSb. In this case, especially optical conductivity spectra pointed to an anisotropic carrier concentration.

The last pnictide in this series is cubic CePdBi [152]. A magnetic phase transition is evident around $T_{\rm c}=2$ K. About 8 % of the sample undergoes a superconducting phase transition close to 1.3 K. It was assumed that this transition was caused by disordered parts of the sample.

3.3 119Sn Mössbauer spectroscopy

The CeTX stannides were additionally characterized through their ¹¹⁹Sn Mössbauer spectra. In many cases, spectra were recorded at liquid nitrogen temperature (in the paramagnetic regime) as well as below the Néel or Curie temperatures. The stannide CeRuSn shows a complex evolution of the spectra as a function of temperature [263]. The spectrum at 323 K could be fitted with one signal at an isomer shift of 1.87 mm s⁻¹. This is the typical range for isomer shifts of stannides [264]. The single signal is indicative of electronically very similar tin atoms in the complex structure of CeRuSn. Already at 298 K and below (at 78 and 4.2 K) a clear distinction of two sets of tin atoms is evident, one with slightly higher and one with slightly lower isomer shift. All spectra showed a clear

quadrupole splitting, reflecting the low site symmetry at the tin atoms. The ¹¹⁹Sn Mössbauer spectra nicely corroborate the recorded ¹¹⁹Sn solid state NMR spectra.

The dimorphism of the stannide CeCuSn [63] is reflected in the \$^{19}\$Sn Mössbauer spectra. The low-temperature phase (\$\alpha\$-CeCuSn) which shows stronger puckering of the Cu_3Sn_3 hexagons reveals slightly higher quadrupole splitting of 0.45 mm s⁻¹ as compared to \$\beta\$-CeCuSn (0.32 mm s⁻¹). Both modifications show magnetic ordering at low temperature. This is expressed in transferred magnetic hyperfine fields of 1.03 T (\$\alpha\$-CeCuSn) and 1.97 T (\$\beta\$-CeCuSn) at the tin nuclei.

CeAgSn [265] shows already a well-resolved quadrupole splitting (1.54 mm s⁻¹) in the 78 K spectrum since the puckering of the Ag₃Sn₃ hexagons is more pronounced than in CeCuSn. The isomer shift of CeAgSn (1.82 mm s⁻¹) is comparable to that of the copper compound. Below the Néel temperature of 8.7 K hyperfine field splitting occurs. Temperature dependent spectra in the magnetically ordered regime show an increasing transferred hyperfine field with decreasing temperature and a maximum field of 2.44 T at 2.2 K. The temperature dependence could be fitted with a Brillouin function and nicely underlined the Néel temperature. Quite similar ¹¹⁹Sn Mössbauer spectroscopic data was obtained for CeAuSn [266]. Only the transferred hyperfine field at 2.05 K is slightly lower (1.24 T), certainly a consequence of a different magnetic structures.

CeZnSn [59] has the highest electron count in the series of CeTSn stannides. This is expressed in a higher isomer shift of 1.97 mm s $^{-1}$ which corresponds to a higher s electron density at the tin nuclei. The 119 Sn spectrum at 4.2 K (only slightly below the Curie temperature of 5.2 K) shows weak broadening of lines due to a small transferred hyperfine field of 0.87 T. Hydrogenation changes the s electron density at the tin nuclei. The isomer shift of CeZnSnH $_{1.5}$ of 1.87 mm s $^{-1}$ is lower (77 K data) [157]. CeZnSnH $_{1.5}$ orders ferromagnetically at the higher Curie temperature of 7.3 K. Thus one detects a higher hyperfine field at 4.2 K. However, the spectrum could only be fitted with a field distribution function which is highly indicative of domain formation in the sample. The average transferred hyperfine field had a value of 2.7 T.

3.4 Hydrogenation behavior

Many CeTX phases have systematically been studied with respect to variations in the magnetic properties, and correlations as a function of the structure and the valence electron count have been established. Especially solid solutions (see chapter 3.5) on the cerium, transition metal

and X sites show the changes in the physical properties as a function of VEC. Another possibility to influence the ground state properties is hydrogenation. This has already been discussed in detail for the ZrNiAl and TiNiSi type phases in the previous two reviews [14, 15]. Many of the CeTX phases described herein also absorb hydrogen but they form different hydride structures. Short overviews on the kinetic sorption behavior, related volume changes and structure–property relations are given in [45, 46].

We start our discussion with hydrides that derive from the tetragonal LaPtSi type CeTX intermetallics. The first candidate is the silicide CePtSi [76] which is one of the rare examples where no hydrogen absorption was observed. The sample showed no decrepitation and the lattice parameters of the hydrogen-treated buttons were close to the precursor product. Isoelectronic CeNiSi however absorbs up to 1.2 equivalents of hydrogen per formula unit [44, 75]. Hydrogenation induces a highly anisotropic variation of the lattice parameters: 407.0 \rightarrow 404.0 pm for the a and 1403.0 \rightarrow 1425.3 pm for the c lattice parameter. Powder neutron diffraction experiments on the deuteride CeNiSiD, revealed two crystallographically independent bipyramidal deuterium sites D@Ce₂Ni₂ and D@Ce₂Si₂, one with partial occupancy. Hydrogenation strongly increases the Kondo interactions in the hydride. Ce $\mathbf{L}_{_{\mathrm{III}}}$ X-ray absorption spectroscopy showed cerium valencies of 3.13 and 3.21 for CeNiSi and its hydride, respectively.

The second family of tetragonal hydrides crystallizes with the well-known ZrCuSiAs type structure [267] which is the parent structure of the huge family of pnictide oxide superconductors. As an example we present in Fig. 12 the structure of the deuteride CeCoGeD [180] whose structure was refined from powder neutron diffraction data. Also the ZrCuSiAs type hydrides show strong anisotropy for the course of the lattice parameters: $417.0 \rightarrow 404.0$ pm for the a and 686.5 \rightarrow 773.5 pm for the c lattice parameter. The strong increase of *c* is a direct consequence of the filling of the tetrahedral voids by hydrogen. Figure 12 shows the alternation of the tetrahedral layers in the CeCoGeD structure. We observe an AB stacking of [CoGe] and [DCe] layers. The strongest bonds within these hydride structures occur for Co-Ge and Ce-H. This is evident from the overlap populations determined from ab initio electronic structure calculations, e.g. for CeCoSiH [268]. Besides CeCoGeD and CeCoGeH, also CeMnGeH, , CeFeSiH, o, and CeCoSiH₁₀ [182] with a full occupancy of the tetrahedral voids by hydrogen have been reported.

The main interest in these quaternary compounds concerns changes in the magnetic ground state properties. For CeCoSi and CeCoGe one observes a transition from

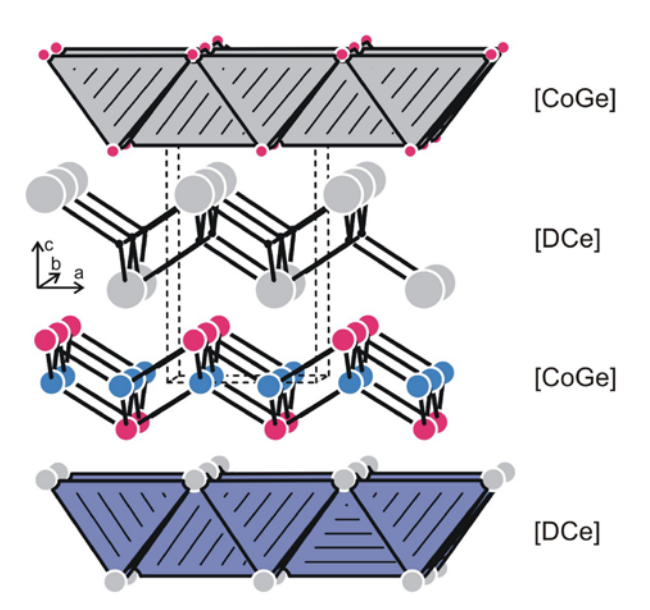


Fig. 12: The crystal structure of CeCoGeD. The D@Ce_{4/4} and Co@ Ge, tetrahedra are drawn in ball-and-stick and in polyhedral representation.

antiferromagnetic to spin fluctuation behavior in going to CeCoSiH and CeCoGeH [180, 268]. Electronic structure calculations for CeCoSi point to an antiferromagnetic ground state with a propagation vector along the *c* axis.

A highly interesting situation occurs for the pair CeMnGe/CeMnGeH. CeMnGe contains two magnetically active atoms, cerium and manganese [182] which lead to antiferromagnetic ordering of manganese at 313 K and of cerium at 41 K. Hydrogenation suppresses the cerium ordering and the manganese substructure of CeMnGeH shows the characteristics of a ferromagnet, a ferrimagnet, or a canted spin system with a Curie temperature of 316 K. This is a direct consequence of the hydrogen insertion into the Ce, tetrahedra.

Hydrogenation certainly also calls for ¹H solid state nuclear magnetic resonance spectroscopic studies. Normally, only samples with the diamagnetic rare earth elements can be tested. A 1H MAS NMR signal with a well resolved sideband pattern was obtained for ZrCuSiAs type LaCoGeH [268], underlining the results of single crystal XRD studies regarding the hydrogen sites. Also the hydrides CeCoSiH and CeCoGeH have been measured (Hahn echo experiments). They both show single signals, however, without sideband patterns. This is a consequence of strong dipolar interactions. The ¹H signal of CeCoGeH is slightly broader than that of CeCoSiH. This coincides with the magnetic behavior. Cerium is in an intermediate valence state in CeCoSiH but nearly trivalent in CeCoGeH. Electronic structure calculations showed stronger Ce–H bonding for CeCoSiH, certainly a consequence of the higher cerium valence.

The hydride CeRuGeH [184] also adopts the ZrCuSiAs type. The hydrogenation destroys the non-magnetic heavy fermion behavior of CeRuGe and induces antiferromagnetic ordering at $T_{\rm N}=4.0$ K in CeRuGeH. At this point is is important to note that CeRuGeH is isoelectronic with the pnictide oxides CeRuPO and CeOsPO [269] which also exhibit ferromagnetic ($T_{\rm C}=15$ K for CeRuPO) and antiferromagnetic ($T_{\rm N}=4.5$ K for CeOsPO) ordering.

Very detailed studies were performed for CeRuSiH [270–272]. Hydrogenation induces antiferromagnetic ordering in the heavy fermion type silicide CeRuSi. Two successive Néel temperatures of $T_{N1} = 7.5$ and $T_{N2} = 3.1$ K were observed for CeRuSiH. Along with specific heat measurements it was possible to derive the magnetic phase diagram for this quaternary hydride. The magnetic structures in the two different antiferromagnetic states were determined from powder neutron diffraction experiments. The cerium magnetic moments show a collinear antiferromagnetic sinusoidal structure between T_{N1} and T_{N2} with a propagation vector $\mathbf{k} = (k_x, k_x, 1/2)$. k_x has a value < 1/3 and tends to the ideal value of 1/3 with decreasing temperature. Approaching T_{N2} , the magnetic structure becomes square wave modulated and commensurate with a propagation vector k = (1/3, 1/3, 1/2). Similar to the isotypic hydrides, strong Ce-H bonding was also evident from ab initio electronic structure calculations of CeRuSiH. Highpressure studies of CeRuSiH in a CuBe piston-cylinder cell up to pressures of 10.3 kbar revealed an increase of both the Néel temperature and the critical field with increasing pressure, in agreement with the Doniach diagram.

The last series of tetragonal hydrides concerns CeScSiH and CeScGeH [185]. Both ternary compounds absorb exactly one equivalent of hydrogen per formula unit. Similar to the ZrCuSiAs type materials discussed above, in CeScSiH and CeScGeH one also observes complete filling of the empty cerium tetrahedra (Fig. 9) by hydrogen. Again, the evolution of the lattice parameters is highly anisotropic: $432.83 \rightarrow 425.4$ pm for the a parameter and 1582.0 \rightarrow 1675.1 pm for the c parameter, in going from CeScSi to CeScSiH. The property changes are drastic. The Néel temperature decreases from 26 to 3.0 K in the sequence CeScSi \rightarrow CeScSiH and from 46 to 3.1 K for CeScGe \rightarrow CeScGeH. The pronounced two-dimensional character of the structural subunits in CeScSiH and CeScGeH is reminiscent of the structural chemistry of layered pnictide oxide materials [267].

Detailed hydrogenation studies were performed for the cubic Laves phase CeMnGa. The quaternary hydrides $CeMnAlH_{1.94}$ and $CeMnAlH_{2.22}$ were reported from detailed

work on the sorption kinetics [118, 119]. Neutron diffraction studies on deuterated samples showed filling of the tetrahedral interstitial sites with hydrogen. Hydrogenation of CeMnGa to CeMnGaH_{1.6} [125] leads to a similar increase of the cubic lattice parameter from 795 to 810 pm.

The last series of hydrides structurally derives from the AlB, type. We can distinguish to structural branches in agreement with the Bärnighausen tree (Fig. 13). The hydrides derive from the YPtAs or the ZrBeSi type. First we discuss the structure of CeZnSnH₁₅ [157]. The stannide CeZnSn can absorb up to 1.5 equivalents of hydrogen per formula unit. Since the hydrogen atoms preferably occupy the Ce₂Zn tetrahedra (as compared to Ce₃Sn; this is evident from ab initio electronic structure calculations), not all sites can simultaneously be occupied because the hydrogen atoms in two face-sharing tetrahedra would be too close. To avoid this repulsion, one fourth of the tetrahedra remains empty (the green squares in Fig. 13) and the ordered model for CeZnSnH_{1.5} shows a symmetry reduction from P6₃/mmc to P6₃mc. The main structural change during the hydrogenation concerns the puckering of the Zn₂Sn₃ hexagons which is only weak in the hydride. Hydrogenation increases the Curie temperature from 4.8 K for CeZnSn to 7.3 K for CeZnSnH_{1.7}. Evaluation of the susceptibility data led to crystal field splitting energies of 519 and 150 cm⁻¹ for E(±1/2) and $E(\pm 3/2)$, respectively.

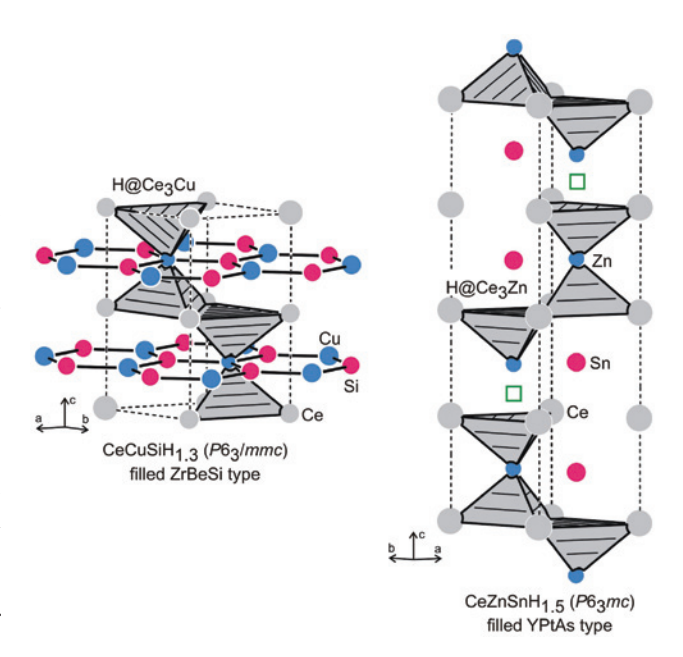


Fig. 13: The crystal structures of CeCuSiH_{1.3} and CeZnSnH_{1.5}. The H@Ce₃Cu and H@Ce₃Zn tetrahedra are emphasized. The green rectangles symbolize empty tetrahedra that cannot simultaneously be occupied.

The hydrides CeCuSiH_{1.3}, CeCuGeH_{1.0}, CeCuGeD_{1.15}, $CeCuSiD_{1.64}$, and $CeCuSnD_{0.33}$ derive from the ZrBeSi type [43, 44, 189, 190, 273]. As an example we present the structure of CeCuSiH, in Fig. 13. The ZrBeSi type allows for a maximum hydrogen content of 2.0 per formula unit for a filling of the tetrahedral voids as marked in that Figure. With reduced hydrogen content various ordering phenomena were observed. These ordered superstructures were determined from electron diffraction and powder neutron diffraction experiments. One observes a direct structure directing influence of the hydrogen insertion. The superstructures show three-fold, five-fold, and seven-fold c axes with respect to the ZrBeSi subcell and consequently can be considered as i3, i5, and i7 isomorphic transitions (in general all prime numbers are allowed) of space group P6/mmc, which are all allowed from a group theoretical point of view. Especially the i7 transition is remarkable. Other important features of these hexagonal hydrides concern the Cu/Sn disorder [273].

Similar to the series of tetragonal phases and their hydrides one also observes changes in the magnetic ground states for the hexagonal phases. While CeCuSi orders ferromagnetically at $T_c = 15.2$ K, a complex series of three subsequent transitions at 13.7, 10.6, and 8.4 K is evident for CeCuSiH_{1,3} [273]. These anomalies were also evident from the real parts of χ'_{AC} measurements. In the sequence $CeCuGe \rightarrow CeCuGeH_{1.0}$, the magnetic ground state changes from ferromagnetic ($T_c = 10.0 \text{ K}$) to nonmagnetic above 1.8 K.

3.5 Solid solutions

Manipulation of the magnetic behavior of a given CeTX compound is possible through the application of external pressure or via hydrogenation, effectively influencing the electronic situation of the cerium atoms. From a chemical point of view it is easy to change the valence electron count through the formation of solid solutions on both the *T* and *X* sites. The magnetic cerium site can be diluted through cerium/lanthanum substitution. Many of such solid solutions show Vegard type behavior for the lattice parameters. The present subchapter lists examples for solid solution on all three sites.

Samples of the complete solid solutions La_vCe_{1-v}MnSi (tetragonal CeFeSi type) were studied with respect to the course of the lattice parameters [274]. Both a and c increase in a linear fashion when cerium is substituted by the larger lanthanum atoms. The silicides show antiferromagnetic ordering of the manganese magnetic moments in the range x = 0-0.5 with a decrease of the Néel temperature from 375 K (x = 0) to 290 K for x = 0.5. A switch to a ferromagnetically ordered state is observed for $x \ge 0.6$ with Curie temperatures around 300 K. In another investigation cerium was substituted by gadolinium. The solid solution Gd_Ce, _MnSi [275] is formed for all x values. The magnetic data are a complex addition of the gadolinium, cerium, and manganese magnetic contributions. Based on detailed temperature dependent susceptibility measurements, the authors could work out the magnetic phase diagram as a function of the cerium/gadolinium substitution.

The third example for cerium/lanthanum substitution concerns Ce, La TiGe [276]. The paramagnetic heavy fermion germanide CeTiGe turns to a more magnetic state and finally towards quantum criticality with increasing lanthanum content.

Now we switch to solid solutions with substitutions on the transition metal sites. The solid solution CeRu, Ni Al was studied in the range of x = 0.1-0.95 [277]. The orthorhombic LaNiAl type is stable up to x = 0.85before the structure switches to the hexagonal ZrNiAl type. The cerium atoms show valence fluctuations over the whole composition range with the tendency towards more trivalent cerium with increasing x. The susceptibility data could be fitted according to the Sales-Wohlleben interconfiguration fluctuation model [278]. XANES data support the model proposed from the magnetic behavior. One of the peculiar structural features of the CeRu, Ni Al solid solution concerns the short Ce-Ru distances which are directly related to the intermediate cerium valence.

A similar switch in structure type was observed for the solid solution CePd, Rh, Al [279]. Already a small amount of 0.2 rhodium equivalents is sufficient to push the solid solution CePd_{1-x}Rh_xAl to the LaNiAl type. The magnetic properties change from antiferromagnetic CePdAl to short-range magnetic ordering in the regime 0 < x < 0.9and finally to another antiferromagnetic state in going to pure CeRhAl. Specific heat and electrical resistivity data indicate spin-glass-like states at low temperature for the samples in the short-range magnetic regime and this is supported by X-ray photoemission spectra.

The platinum atoms in CePtSi (LaPtSi type) can stepwise be substituted by nickel. The course of the lattice parameters in the solid solution CePt, Ni, Si [280] shows almost Vegard type behavior. An anomaly in the a parameter around x = 0.5 is the consequence of a transition from heavy fermion behavior to a mixed-valence state. This transition is evident from susceptibility, resistivity [280], and specific heat data [281]. A second study was devoted to platinum substitution by gold [282, 283]. This solid solution was investigated up to 20 % gold content.

The substitution mainly influences the c lattice parameter. Based on high-resolution resistivity measurements, increasing gold content leads to a smooth change from a coherent Kondo lattice state to a single-impurity Kondo behavior. Specific heat data indicate a more enhanced heavy fermion state for CePt, 94Au, 06Si as compared to CePtSi [282].

An interesting solid solution was studied for the germanide CeCuGe. Up to 50 % of the copper atoms can be substituted by aluminum, keeping the ZrBeSi type structure intact. With increasing aluminum concentration the c parameter of $CeCu_{1-x}Al_xGe$ shows a strong increase from 807.9 pm for x = 0.1 to 851.0 pm for x = 0.5 [284]. The copper-aluminum mixing induces some disorder within the puckered hexagons. This is reflected in the susceptibility measurements. The Curie temperature decreases from 11.1 K for x = 0.1 to 5.6 K for x = 0.5. All samples show a slightly enhanced moment of 2.7 \pm 0.1 $\mu_{\scriptscriptstyle R}$ per formula unit. Resistivity measurements show the usual Kondo minimum and a sharp decrease at T_c due to reduced spindisorder scattering.

Several solid solutions were studied for the intermediate valence stannide CeRuSn. Since this peculiar crystal structure is directly related to the short Ce-IV-Ru distances, within the solid solution Ce, La, RuSn [285] it is only possible to substitute half on the cerium atoms (i.e. trivalent cerium) by lanthanum. This was confirmed by the experiment. The cerium-lanthanum substitution led to a collapse of the superstructure for x = 0.3 and the lanthanum-richer samples crystallize with the CeCoAl subcell structure. This was confirmed through the absence of superstructure reflections in both powder and single crystal X-ray diffraction data. The intermediate cerium valence was underlined by XANES spectra. The complete solid solutions CeRu, Rh, Sn [286], CeRu, Ni, Sn [287], and CeRu,_Pd, Sn [288] were also studied. For all three series it was evident that the CeRuSn structure allows only for tiny degrees of ruthenium substitution by another transition metal. Already at small x values one observes a switch into another structure type. This data was already discussed in the previous reviews [14, 15].

Detailed data is also available for solid solutions that derive from the antimonide CePdSb. The cerium atoms can stepwise be substituted by diamagnetic lanthanum, leading to a dilution of the magnetic substructure [289]. This dilution has a direct influence on the ferromagnetic ground state. The Curie temperature in Ce,_La,PdSb decreases from 17.5 K for x = 0 to 3.8 K for x = 0.7, while samples with higher lanthanum content do not show magnetic ordering. In parallel one observes a strong decrease of the saturation magnetization. The shift in the Curie temperature is also evident in the resistivity measurements. XPS spectra suggest hybridization of the f states with the conduction electrons.

Substitution of the palladium by platinum atoms leads to Vegard type behavior [290] with a slight decrease of a and c with increasing x in CePd, Pt,Sb. Palladiumplatinum substitution leads to a strong drop of the Curie temperature and the platinum end member has $T_c = 4.8 \text{ K}$. The ferromagnetic ordering switches from a low-dimensional one in CePdSb to a normal three-dimensional one in CePtSb. CePdSn also tolerates some palladium-rhodium substitution [291, 292]

The last family of solid solution concerns substitutions on the X site. The silicon position of the heavy fermion silicide CePtSi can be substituted by small amounts of germanium. CePtSi, Ge, has been studied up to the composition CePtSb_{0.8}Ge_{0.2} [293–296]. The silicongermanium substitution pushes the heavy fermion state to an antiferromagnetic ground state. The switch in the magnetic behavior was monitored in parallel by ²⁹Si solid state NMR spectroscopy.

4 Summary

The many CeTX phases that crystallize with structures other than the ZrNiAl and TiNiSi type show a manifold of crystal structures that give rise to distinctly different magnetic and electrical properties. Although the lists of references in the three review [14, 15] are long, Fig. 1 still leaves some white spots and nicely demonstrates the synthetic potential of this family of compounds for the future. The understanding of the complex interplay of structures and properties is a fruitful interdisciplinary task for chemists and physicists.

Acknowledgments: This work was supported by the Deutsche Forschungsgemeinschaft.

References

- [1] E. Parthé, L. Gelato, B. Chabot, M. Penzo, K. Cenzual, R. Gladyshevskii, TYPIX-Standardized Data and Crystal Chemical Characterization of Inorganic Structure Types. Gmelin Handbook of Inorganic and Organometallic Chemistry, 8th ed., Springer, Berlin, 1993.
- [2] A. Szytuła, J. Leciejewicz, Handbook of Crystal Structures and Magnetic Properties of Rare Earth Intermetallics, CRC Press, Boca Raton, 1994.
- [3] M. L. Fornasini, F. Merlo, J. Alloys Compd. 1995, 219, 63.

- [4] S. F. Matar, Progr. Solid State Chem. 2013, 41, 55.
- [5] P. Villars, K. Cenzual, Pearson's Crystal Data: Crystal Structure Database for Inorganic Compounds (release 2015/16), ASM International®, Materials Park, Ohio (USA), 2015.
- [6] S. Gupta, K. G. Suresh, J. Alloys Compd. 2015, 618, 562.
- [7] R. Pöttgen, D. Johrendt, Chem. Mater. 2000, 12, 875.
- [8] R. Pöttgen, D. Johrendt, D. Kußmann in Handbook on the Physics and Chemistry of Rare Earths, Vol. 32 (Eds.: K. A. Gschneidner Jr., J.-C. Bünzli), North-Holland/Elsevier, Amsterdam, 2001, chapter 207, p. 453.
- [9] G. R. Stewart, Rev. Mod. Phys. 2006, 78, 743.
- [10] R. Settai, T. Takeuchi, Y. Ōnuki, J. Phys. Soc. Jpn. 2007, 76, 051003.
- [11] H. von Löhneysen, A. Rosch, M. Vojta, P. Wölfle, Rev. Mod. Phys. 2007, 79, 1015.
- [12] P. Gegenwart, Q. Si, F. Steglich, Nature Phys. 2008, 4, 186.
- [13] O. Stockert, S. Kirchner, F. Steglich, Q. Si, J. Phys. Soc. Jpn. 2012, 81, 011001.
- [14] R. Pöttgen, B. Chevalier, Z. Naturforsch. 2015, 70b, 289.
- [15] O. Janka, O. Niehaus, R. Pöttgen, B. Chevalier, Z. Naturforsch. 2016, 71b, in press.
- [16] R. Pöttgen, Th. Gulden, A. Simon, GIT Labor-Fachzeitschrift **1999**, 43, 133.
- [17] R. Ferro, A. Saccone, Intermetallic Chemistry, Elsevier, Amsterdam, 2008.
- [18] R. Pöttgen, D. Johrendt, Intermetallics, De Gruyter, Berlin,
- [19] L. D. Gulay, M. Wołcyrz, J. Alloys Compd. 2001, 316, 209.
- [20] A. Provino, D. Paudyal, A. V. Morozkin, P. Manfrinetti, K. A. Gschneidner Jr., J. Alloys Compd. 2014, 587, 783.
- [21] C. Ritter, S. K. Dhar, R. Kulkarni, A. Provino, D. Paudyal, P. Manfrinetti, K. A. Gschneidner, J. Phys.: Condens. Matter 2014, 26, 366001.
- [22] J. Emsley, The Elements, Oxford University Press, Oxford 1999.
- [23] R. Welter, G. Venturini, B. Malaman, E. Ressouche, J. Alloys Compd. 1993, 202, 165.
- [24] J. D. Corbett, A. Simon, Inorg. Synth. 1983, 22, 15.
- [25] S. K. Dhar, P. Manfrinetti, A. Palenzona, Phys. Rev. B 1995, 51,
- [26] W. Hermes, S. Rayaprol, R. Pöttgen, Z. Naturforsch. 2007, 62b, 901.
- [27] A. Provino, K. A. Gschneidner Jr., P. Manfrinetti, J. Alloys Compd. 2010, 497, 131.
- [28] D. Kußmann, R.-D. Hoffmann, R. Pöttgen, Z. Anorg. Allg. Chem. **1998**, 624, 1727.
- [29] R. Pöttgen, A. Lang, R.-D. Hoffmann, B. Künnen, G. Kotzyba, R. Müllmann, B. D. Mosel, C. Rosenhahn, Z. Kristallogr. 1999, 214,
- [30] S. Singh, S. K. Dhar, C. Mitra, P. Paulose, P. Manfrinetti, A. Palenzona, J. Phys.: Condens. Matter 2001, 13, 3753.
- [31] D. Niepmann, Yu. M. Prots', R. Pöttgen, W. Jeitschko, J. Solid State Chem. 2000, 154, 329.
- [32] M. G. Kanatzidis, R. Pöttgen, W. Jeitschko, Angew. Chem. Int. Ed. 2005, 44, 6996.
- [33] S. Chang, Y. Janssen, V. O. Garlea, J. Zarestky, H. Nakotte, R. J. McQueeney, J. Appl. Phys. 2005, 97, 10A913.
- [34] M. Sera, T. Satoh, T. Kasuya, J. Phys. Soc. Jpn. 1988, 57, 671.
- [35] Y. Uwatoko, M. Kosaka, T. Sigeoka, *Physica B* **1999**, *259–261*, 114.
- [36] J. Fikáček, J. Prokleška, M. Mišek, J. Custers, S. Daniš, J. Prchal, V. Sechovský, I. Císařová, Phys. Rev. B 2012, 86, 054108.

- [37] R. Feyerherm, E. Dudzik, S. Valencia, J. A. Mydosh, Y.-K. Huang, W. Hermes, R. Pöttgen, Phys. Rev. B 2012, 85, 085120.
- [38] A. Prokofiev, S. Paschen in Modern Aspects of Bulk Crystal and Thin Film Preparation, (Eds.: N. Kolesnikov, E. Borisenko), Intechopen, 2012, chapter 11, DOI: 10.5772/29675.
- [39] S. Yoshii, H. Suzuki, D. Tazawa, M. Kasaya, J. Phys. Soc. Jpn. **1997**, 66, 2569.
- [40] K. Katoh, A. Ochiai, T. Suzuki, Physica B 1996, 223-224, 340.
- [41] K. Katoh, T. Takabatake, I. Oguro, A. Ochiai, A. Uesawa, T. Suzuki, J. Phys. Soc. Jpn. 1999, 68, 613.
- [42] T. Iwasaki, A. Sekiyama, A. Yamasaki, M. Okazaki, K. Kadono, H. Utsunomiya, S. Imada, Y. Saitoh, T. Muro, T. Matsushita, H. Harima, S. Yoshii, M. Kasaya, A. Ochiai, T. Oguchi, K. Katoh, Y. Niide, K. Takegahara, S. Suga, Phys. Rev. B 2002, 65, 195109.
- [43] J. P. Maehlen, M. Stange, V. A. Yartys, R. G. Delaplane, J. Alloys Compd. 2005, 404-406, 112.
- [44] F. Weill, M. Pasturel, J.-L. Bobet, B. Chevalier, J. Phys. Chem. Solids 2006, 67, 1111.
- [45] J.-L. Bobet, M. Pasturel, B. Chevalier, Intermetallics 2006, 14,
- [46] B. Chevalier, S. Tencé, E. Gaudin, S. F. Matar, J.-L. Bobet, J. Alloys Compd. 2009, 480, 43.
- [47] R.-D. Hoffmann, R. Pöttgen, Z. Kristallogr. 2001, 216, 127.
- [48] R. Pöttgen, Z. Anorg. Allg. Chem. 2014, 640, 869.
- [49] H. Bärnighausen, Commun. Math. Chem. 1980, 9, 139.
- [50] U. Müller, Z. Anorg. Allg. Chem. 2004, 630, 1519.
- [51] U. Müller in International Tables for Crystallography, Symmetry Relations between Space Groups, Vol. A1 (Eds.: H. Wondratschek, U. Müller), 2nd ed., John Wiley & sons, Ltd, Chichester, 2010, p. 44.
- [52] U. Müller, Symmetriebeziehungen zwischen verwandten Kristallstrukturen, Vieweg + Teubner Verlag, Wiesbaden, 2012.
- [53] G. Wenski, A. Mewis, Z. Kristallogr. 1986, 176, 125.
- [54] J. W. Nielsen, N. C. Baenziger, Acta Crystallogr. 1954, 7, 132.
- [55] W. Bockelmann, H. Jacobs, H.-U. Schuster, Z. Naturforsch. 1970, 25b, 1305.
- [56] G. Wenski, A. Mewis, Z. Anorg. Allg. Chem. 1986, 535, 110.
- [57] V. Babizhets'ky, C. Le Sénéchal, J. Bauer, S. Députier, R. Guérin, J. Alloys Compd. 1999, 287, 174.
- [58] A. landelli, Z. Anorg. Allg. Chem. 1964, 330, 221.
- [59] W. Hermes, S. F. Matar, T. Harmening, U. Ch. Rodewald, M. Eul, R. Pöttgen, Z. Naturforsch. 2009, 64b, 175.
- [60] D. Johrendt, A. Mewis, Z. Naturforsch. 1990, 45b, 1262.
- [61] D. Niepmann, R. Pöttgen, K. M. Poduska, F. J. DiSalvo, H. Trill, B. D. Mosel, Z. Naturforsch. 2001, 56b, 1.
- [62] R. Pöttgen, H. Borrmann, C. Felser, O. Jepsen, R. Henn, R. K. Kremer, A. Simon, J. Alloys Compd. 1996, 235, 170.
- [63] C. P. Sebastian, S. Rayaprol, R.-D. Hoffmann, U. Ch. Rodewald, T. Pape, R. Pöttgen, Z. Naturforsch. 2007, 62b, 647.
- [64] V. Brouskov, M. Hanfland, R. Pöttgen, U. Schwarz, Z. Kristallogr. 2005, 220, 122.
- [65] G. Cordier, G. Dörsam, R. Kniep, J. Magn. Magn. Mater. 1988, *76-77*, 653.
- [66] C. B. Shoemaker, D. P. Shoemaker, Acta Crystallogr. 1965, 18, 900.
- [67] P. I. Krypyakevich, V. Ya. Markiv, E. V. Melnyk, Dopov. Akad. Nauk. Ukr. RSR Ser. A 1967, 750.
- [68] A. E. Dwight, M. H. Mueller, R. A. Conner Jr., J. W. Downey, H. Knott, Trans. Met. Soc. AIME 1968, 242, 2075.

- [69] M. F. Zumdick, R.-D. Hoffmann, R. Pöttgen, Z. Naturforsch. 1999, 54b, 45.
- [70] W. Hermes, A. F. Al Alam, S. F. Matar, R. Pöttgen, Solid State Sci. 2008, 10, 1895.
- [71] A. V. Gribanov, A. I. Tursina, A. V. Grytsiv, E. V. Murashova, N. G. Bukhan'ko, P. Rogl, Y. D. Seropegin, G. Giester, J. Alloys Compd. 2008, 454, 164.
- [72] A. Gribanov, A. Tursina, E. Murashova, Y. Seropegin, E. Bauer, H. Kaldarar, R. Lackner, H. Michor, E. Royanian, M. Reissner, P. Rogl, J. Phys.: Condens. Matter 2006, 18, 9593.
- [73] O. Niehaus, O. Janka, Z. Anorg. Allg. Chem. 2015, 641, 1792.
- [74] H. H. Hill in Plutonium and Other Actinides, Nuclear Materials Series, (Ed. W. N. Mines), The Metallurgical Society of AIME, New York, 1970, 17, 2.
- [75] M. Pasturel, F. Weill, F. Bourée, J.-L. Bobet, B. Chevalier, J. Alloys Compd. 2005, 397, 17.
- [76] W. Hermes, U. Ch. Rodewald, B. Chevalier, R. Pöttgen, Z. Naturforsch. 2007, 62b, 613.
- [77] T. Sasakawa, T. Suemitsu, J. Kitagawa, O. Sologub, P. Salamakha, T. Takabatake, J. Phys.: Condens. Matter 2002, 14, L267.
- [78] A. Löhken, G. J. Reiß, D. Johrendt, A. Mewis, Z. Anorg. Allg. Chem. 2005, 631, 1144.
- [79] K. Klepp, E. Parthé, Acta Crystallogr. 1982, B38, 1105.
- [80] G. Brauer, A. Mitius, Z. Anorg. Allg. Chem. 1942, 249, 325.
- [81] A. Lipatov, A. Gribanov, A. Grytsiv, S. Safronov, P. Rogl, J. Rousnyak, Y. Seropegin, G. Giester, J. Solid State Chem. 2010, 183, 829.
- [82] B. Heying, R. Pöttgen, M. Valldor, U. Ch. Rodewald, R. Mishra, R.-D. Hoffmann, Monatsh. Chem. 2004, 135, 1335.
- [83] K. Klepp, E. Parthé, Acta Crystallogr. B 1982, 38, 1541.
- [84] K.-H. Janzon, H. Schäfer, A. Weiss, Angew. Chem. 1965, 77, 258.
- [85] Yu. M. Prots', W. Jeitschko, M. Gerdes, B. Künnen, Z. Anorg. Allg. Chem. 1998, 624, 1855.
- [86] W. Hermes, S. Linsinger, R. Mishra, R. Pöttgen, Monatsh. Chem. 2008, 139, 1143.
- [87] M. G. Haase, T. Schmidt, C. G. Richter, H. Block, W. Jeitschko, J. Solid State Chem. 2002, 168, 18.
- [88] H. Nowotny, W. Sibert, Z. Metallkd. 1941, 33, 391.
- [89] H. Lin, L. A. Wray, Y. Xia, S. Xu, S. Jia, R. J. Cava, A. Bansil, M. Z. Hasan, Nat. Mater. 2010, 9, 546.
- [90] R. Welter, G. Venturini, B. Malaman, J. Alloys Compd. 1994, 206, 55.
- [91] O. I. Bodak, E. I. Gladyshevskii, A. V. Kardash, E. E. Cherkashin, Inorg. Mater. 1970, 6, 935.
- [92] W. N. Stassen, M. Sato, L. D. Calvert, Acta Crystallogr. B 1970, 26, 1534.
- [93] A. V. Morozkin, Yu. D. Seropegin, I. A. Sviridov, J. Alloys Compd. 1999, 285, L5.
- [94] R. Welter, G. Venturini, E. Ressouche, B. Malaman, J. Alloys Compd. 1994, 210, 279.
- [95] Yu. N. Grin', O. M. Sichevich, V. A. Bruskov, R. M. Rykhal', Ya. P. Yarmolyuk, Sov. Phys. Crystallogr. 1983, 28, 346.
- [96] J. Goraus, A. Ślebarski, M. Fijałkowski, Intermetallics 2013, 32, 219.
- [97] J. F. Riecken, W. Hermes, B. Chevalier, R.-D. Hoffmann, F. M. Schappacher, R. Pöttgen, Z. Anorg. Allg. Chem. 2007, 633, 1094.
- [98] V. Gribanova, E. Murashova, Yu. Seropegin, A. Gribanov, J. Alloys Compd. 2014, 585, 352.
- [99] W. Hermes, S. F. Matar, R. Pöttgen, Z. Naturforsch. 2009, 64b, 901.

- [100] T. Mishra, R.-D. Hoffmann, C. Schwickert, R. Pöttgen, Z. Naturforsch. 2011, 66b, 771.
- [101] S. F. Matar, J. F. Riecken, B. Chevalier, R. Pöttgen, A. F. Al Alam, V. Eyert, Phys. Rev. B 2007, 76, 174434.
- [102] J. A. Mydosh, A. M. Strydom, M. Baenitz, B. Chevalier, W. Hermes, R. Pöttgen, Phys. Rev. B 2011, 83, 054411.
- [103] K. Prokeš, J. A. Mydosh, O. Prokhnenko, W.-D. Stein, S. Landsgesell, W. Hermes, R. Feyerherm, R. Pöttgen, Phys. Rev. B 2013, 87, 094421.
- [104] J. Fikáček, J. Prchal, J. Prokleška, I. Císařová, V. Sechovsý, Solid State Phen. 2013, 194, 40.
- [105] J. Fikáček, J. Prokleška, J. Prchal, J. Custers, V. Sechovský, J. Phys.: Condens. Matter 2013, 25, 416006.
- [106] K. Prokeš, V. Petříček, E. Ressouche, S. Hartwig, B. Ouladdiaf, J. A. Mydosh, R.-D. Hoffmann, Y.-K. Huang, R. Pöttgen, J. Phys.: Condens. Matter 2014, 26, 122201.
- [107] K. Prokeš, S. A. J. Kimber, J. A. Mydosh, R. Pöttgen, Phys. Rev. B 2014, 89, 064106.
- [108] R. Feyerherm, E. Dudzik, K. Prokeš, J. A. Mydosh, Y.-K. Huang, R. Pöttgen, Phys. Rev. B 2014, 90, 041104.
- [109] K. Prokeš, S. Hartwig, A. Gukasov, J. A. Mydosh, Y.-K. Huang, O. Niehaus, R. Pöttgen, Phys. Rev. B 2015, 91, 014424.
- [110] O. S. Zarechnyuk, R. M. Ryjkal', V. V. Korin, Dopov. Akad. Nauk Ukr. RSR, Ser. A 1980, 84.
- [111] Q. Yao, H. Zhou, C. Tang, S. Pan, J. Rare Earths 2011, 29, 650.
- [112] N. Nasri, J. Gastebois, M. Pasturel, B. Belgacem, I. Péron, F. Gouttefangeas, R. Ben Hassen, O. Tougait, H. Noël, J. Alloys Compd. 2015, 628, 277.
- [113] A. L. Shilov, Russ. J. Phys. Chem. 1987, 61, 719.
- [114] M. C. Gao, N. Ünlü, M. Mihalkovic, M. Widom, G. J. Shiflet, Met. Mater. Trans. A 2007, 38A, 2540.
- [115] A. Ślebarski, J. Goraus, A. Hackemer, M. Sołyga, Phys. Rev. B 2004, 70, 195123.
- [116] N. H. Kumar, S. K. Malik, Phys. Rev. B 2000, 62, 127.
- [117] H. Schwer, F. Hulliger, J. Alloys Compd. 1997, 259, 249.
- [118] P. Spatz, K. J. Gross, A. Züttel, F. Fauth, P. Fischer, L. Schlapbach, J. Alloys Compd. 1997, 261, 263.
- [119] P. Spatz, K. J. Gross, A. Züttel, L. Schlapbach, J. Alloys Compd. **1997**, 260, 211.
- [120] A. V. Morozkin, J. Alloys Compd. 2004, 370, L1.
- [121] D. Berthebaud, O. Tougait, M. Potel, H. Noël, J. Alloys Compd. 2007, 442, 104.
- [122] R. Welter, I. Ijjaali, G. Venturini, B. Malaman, J. Alloys Compd. 1998, 265, 196.
- [123] M. Lenkewitz, S. Corsépius, G. R. Stewart, J. Alloys Compd. 1996, 241, 121.
- [124] J. H. V. Brabers, F. R. de Boer, K. H. J. Buschow, J. Alloys Compd. 1992, 179, 227.
- [125] B. Chevalier, J.-L. Bobet, M. Pasturel, E. Gaudin, J. Etourneau, J. Alloys Compd. 2003, 356-357, 147.
- [126] D. Mazzone, D. Rossi, R. Marazza, R. Ferro, J. Less-Common Met. 1982, 84, 301.
- [127] D. Rossi, R. Marazza, D. Mazzone, R. Ferro, J. Less-Common Met. 1981, 78, P1.
- [128] H. Kido, T. Hoshikawa, M. Tagami, M. Shimada, M. Koizumi, Yogyo Kyokai Shi 1986, 94, 242.
- [129] R. Marazza, D. Rossi, R. Ferro, Gazz. Chim. Ital. 1980, 110,
- [130] P. S. Salamakha, M. B. Konyk, R. Dzyanyi, O. I. Sologub, O. I. Bodak, Pol. J. Chem. 1996, 70, 270.

- [131] R. Welter, A. Vernière, G. Venturini, B. Malaman, J. Alloys Compd. 1999, 283, 54.
- [132] W. Rieger, E. Parthé, Monatsh. Chem. 1969, 100, 439.
- [133] W. Hermes, R. Pöttgen, Z. Naturforsch. 2009, 64b, 361.
- [134] E. Cordruwisch, D. Kaczorowski, A. Saccone, P. Rogl, R. Ferro, J. Phase Eq. 1999, 20, 407.
- [135] B. M. Mhlungu, A. M. Strydom, Physica B 2008, 403, 862.
- [136] R. Pöttgen, H. Borrmann, R. K. Kremer, J. Magn. Magn. Mater. 1996, 152, 196,
- [137] A. landelli, J. Alloys Compd. 1993, 187, 141.
- [138] Yu. D. Seropegin, B. I. Shapiev, A. V. Gribanov, O. I. Bodak, J. Alloys Compd. 1999, 288, 155.
- [139] R. Welter, G. Venturini, B. Malaman, E. Ressouche, J. Alloys Compd. 1993, 201, 191.
- [140] B. M. Sondezi-Mhlungu, D. T. Adroja, A. M. Strydom, S. Paschen, E. A. Goremychkin, Physica B 2009, 404, 3032.
- [141] B. Chevalier, B. Malaman, Solid State Commun. 2004, 130, 711.
- [142] V. K. Pecharsky, K. A. Gschneidner Jr., O. I. Bodak, A. S. Protsyk, J. Less-Common Met. 1991, 168, 257.
- [143] B. Chevalier, W. Hermes, E. Gaudin, R. Pöttgen, J. Phys.: Condens. Matter 2010, 22, 146003.
- [144] M. Deppe, N. Caroca-Canales, S. Hartmann, N. Oelscher, C. Geibel, J. Phys.: Condens. Matter 2009, 21, 206001.
- [145] S. Ramakrishnan, K. Ghosh, A. D. Chinchure, V. R. Marathe, G. Chandra, Phys. Rev. B 1995, 52, 6784.
- [146] B. Belan, O. Bodak, R. Gladyshevskii, I. Soroka, B. Kuzhel, O. Protsyk, I. Stets, J. Alloys Compd. 2005, 396, 212.
- [147] A. V. Gribanov, Y. D. Seropegin, A. I. Tursina, O. I. Bodak, P. Rogl, H. Noël, J. Alloys Compd. 2004, 383, 286.
- [148] W. H. Lee, R. N. Shelton, Phys. Rev. B 1987, 35, 5369.
- [149] R. Welter, G. Venturini, B. Malaman, J. Alloys Compd. 1992, 189, 49.
- [150] D. Johrendt, A. Mewis, J. Alloys Compd. 1992, 183, 210.
- [151] W. Jeitschko, L. J. Terbüchte, U. Ch. Rodewald, Z. Naturforsch. 2001, 56b, 1281.
- [152] J. Goraus, A. Ślebarski, M. Fijałkowski, J. Phys.: Condens. Matter 2013, 25, 176002.
- [153] R. Marazza, D. Rossi, R. Ferro, J. Less-Common Met. 1988, 138, 189,
- [154] D. Mazzone, G. Borzone, D. Rossi, R. Ferro, J. Less-Common Met. 1983, 94, L5.
- [155] W. Hermes, U. Ch. Rodewald, B. Chevalier, S. F. Matar, V. Eyert, R. Pöttgen, Solid State Sci. 2010, 12, 929.
- [156] L. D. Gulay, J. Alloys Compd. 2002, 347, 124.
- [157] W. Hermes, B. Chevalier, U. Ch. Rodewald, S. F. Matar, F. Weill, I. Schellenberg, R. Pöttgen, H. Lueken, M. Speldrich, Chem. Mater. 2011, 23, 1096.
- [158] K. Katoh, G. Terui, Y. Niide, A. Oyamada, A. Ochiai, J. Alloys Compd. 2002, 339, 236.
- [159] S. I. Chikhrii, S. V. Orishchin, Yu. B. Kuz'ma, Russ. J. Inorg. Chem. 1987, 32, 1386.
- [160] J. Liang, Y. Han, Y. Ouyang, S. Xie, J. Meng, L. Zhu, M. Ling, J. Rare Earths 2012, 30, 916.
- [161] P. Manfrinetti, M. Pani, J. Alloys Compd. 2005, 393, 180.
- [162] F. Yang, J. P. Kuang, J. Li, E. Brück, H. Nakotte, F. R. de Boer, X. Wu, Z. Li, Y. Wang, J. Appl. Phys. 1991, 69, 4705.
- [163] P. Boulet, D. Mazzone, H. Noël, P. Riani, P. Rogl, R. Ferro, Intermetallics 1999, 7, 931.
- [164] P. Boulet, D. Mazzone, H. Noël, P. Rogl, R. Ferro, J. Alloys Compd. 2001, 317-318, 350.

- [165] P. Riani, D. Mazzone, G. Zanicchi, R. Marazza, R. Ferro, F. Faudot, M. Harmelin, J. Phase Eq. 1998, 19, 239.
- [166] K. Hartjes, W. Jeitschko, J. Alloys Compd. 1995, 226, 81.
- [167] R. V. Skolozdra, Ja. F. Mikhalski, K. Kaczmarska, J. Pierre, J. Alloys Compd. 1994, 206, 141.
- [168] L. Menon, S. K. Dhar, S. K. Malik, W. B. Yelon, J. Appl. Phys. 1996, 79, 6367.
- [169] S. K. Malik, D. T. Adroja, J. Magn. Magn. Mater. 1991, 102, 42.
- [170] R. Marazza, D. Rossi, R. Ferro, J. Less-Common Met. 1980, 75,
- [171] A. Zygmunt, A. Szytuła, J. Alloys Compd. 1995, 219, 185.
- [172] B. D. Rainford, D. T. Adroja, Physica B 1994, 194-196, 365.
- [173] L. Menon, S. K. Malik, Phys. Rev. B 1995, 52, 35.
- [174] V. K. Pecharskii, Yu. V. Pankevich, O. I. Bodak, Sov. Phys. Crvstalloar, 1983, 28, 97.
- [175] K. Katoh. T. Takabatake, A. Ochiai, A. Uesawa, T. Suzuki, Physica B 1997, 230-232, 159.
- [176] I. Karla, J. Pierre, B. Ouladdiaf, Physica B 1998, 253, 215.
- [177] I. Karla, J. Pierre, R. V. Skolozdra, J. Alloys Compd. 1998,
- [178] P. C. Canfield, J. D. Thompson, W. P. Beyermann, A. Lacerda, M. F. Hundley, E. Peterson, Z. Fisk, H. R. Ott, J. Appl. Phys. **1991**, 70, 5800.
- [179] M. Pasturel, J.-L. Bobet, O. Isnard, B. Chevalier, J. Alloys Compd. 2004, 384, 39.
- [180] B. Chevalier, E. Gaudin, F. Weill, J.-L. Bobet, Intermetallics 2004, 12, 437.
- [181] B. Chevalier, S. F. Matar, Phys. Rev. B 2004, 70, 174408.
- [182] B. Chevalier, M. Pasturel, J.-L. Bobet, O. Isnard, Solid State Commun. 2005, 134, 529.
- [183] B. Chevalier, E. Gaudin, S. Tencé, B. Malaman, J. Rodriguez Fernandez, G. André, B. Coqblin, Phys. Rev. B 2008, 77, 014414.
- [184] B. Chevalier, E. Gaudin, C. Geibel, N. C. Canales, W. Hermes, R. Pöttgen, J. Phys.: Condens. Matter 2010, 22, 046003.
- [185] B. Chevalier, W. Hermes, B. Heying, U. Ch. Rodewald, A. Hammerschmidt, S. F. Matar, E. Gaudin, R. Pöttgen, Chem. Mater. 2010, 22, 5013.
- [186] I. R. Mokra, O. I. Bodak, Dopov. Akad. Nauk Ukr. RSR, Ser. A **1979**, 4, 312.
- [187] O. I. Bodak, Z. M. Kokhan, Inorg. Mater. 1983, 19, 987.
- [188] S. N. Mishra, J. Phys.: Condens. Matter 2009, 21, 115601.
- [189] M. Pasturel, F. Weill, J.-L. Bobet, Z. Naturforsch. 2007, 62b,
- [190] B. Chevalier, M. Pasturel, J.-L. Bobet, F. Weill, R. Decourt, J. Etourneau, J. Solid State Chem. 2004, 177, 752.
- [191] A. E. Dwight, Proc. 12th Rare Earth Res. Conf., Colorado, 1976,
- [192] R. Settai, Y. Yoshida, A. Yamaguchi, Y. Ōnuki, S. Yoshii, M. Kasaya, H. Harima, K. Takegahara, J. Phys. Soc. Jpn. 1999, 68,
- [193] S. Yoshii, M. Kasaya, H. Osaka, H. Suzuki, JJAP Series 1999, 11, 132,
- [194] O. Niehaus, R.-D. Hoffmann, S. Tencé, B. Chevalier, R. Pöttgen, Z. Kristallogr. 2015, 230, 579.
- [195] O. Niehaus, R.-D. Hoffmann, B. Chevalier, R. Pöttgen, Z. Kristallogr. 2016, 231, DOI: 10.1515/zkri-2015-1882.
- [196] P. K. Nikolok, Metallofiz. Nov. Tekhnol. 2001, 23, 431.
- [197] Y. Tagawa, K. Inaba, J. Sakurai, Y. Komura, Solid State Commun. 1988, 66, 993.

- [198] J. Sakurai, K. Inaba, J. Schweizer, Solid State Commun. 1993, 87, 1073.
- [199] P. C. Canfield, J. D. Thompson, Z. Fisk, J. Appl. Phys. 1991, 70, 5992.
- [200] T. Shigeoka, M. Yokoyama, M. Kosaka, Y. Uwatoko, M. Furugen, S. Ishida, S. Asano, *Physica B* **2000**, *281–282*, 96.
- [201] Y. Uwatoko, T. Ishii, G. Oomi, H. Takahashi, N. Mori, S. Nimori, G. Kido, J. L. Sarrao, D. Mandrus, Z. Fisk, J. D. Thompson, Physica B 1997, 237-238, 207.
- [202] M. Deppe, N. Caroca-Canales, J. G. Sereni, C. Geibel, J. Phys.: Conf. Ser. 2010, 200, 012026.
- [203] M. Deppe, S. Lausberg, F. Weickert, M. Brando, Y. Skourski, N. Caroca-Canales, C. Geibel, F. Steglich, Phys. Rev. B 2012, 85, 060401.
- [204] V. A. Romaka, O. M. Sichevich, R. E. Gladyshevskiy, Ya. P. Yarmolyuk, Yu. N. Grin, Phys. Met. Metall. 1983, 56, 53.
- [205] M. D. Koterlin, B. S. Morokhivski, Yu. N. Grin, O. M. Sichevich, Dopov. Akad. Nauk Ukr. RSR, Ser. A 1988, 11, 70.
- [206] M. D. Koterlyn, B. S. Morokhivski, I. D. Shcherba, L. J. Živković, R. V. Lutsiv, J. Serb. Chem. Soc. 1991, 56, 733.
- [207] N. Harish Kumar, S. K. Malik, Solid State Commun. 2000, 114, 223.
- [208] C. L. Dong. K. Asokan, C. L. Chen, C. L. Chang, W. F. Pong, N. Harish Kumar, S. K. Malik, *Physica B* **2003**, *325*, 235.
- [209] M. Sera, T. Satoh, T. Kasuya, J. Phys. Soc. Jpn. 1987, 56,
- [210] A. Hamzic, A. Fert, M. Miljak, S. Horn, Phys. Rev. B 1988, 38, 7141.
- [211] L. Rebelsky, K. Reilly, S. Horn, H. Borges, J. D. Thompson, J. O. Willis, R. Aikin, R. Caspari, C. D. Bredl, J. Appl. Phys. **1988**, 63, 3405.
- [212] R. Köhler, B. Strobel, C. Kämmerer, A. Grauel, U. Gottwick, E. Göring, A. Höhr, G. Sparn, C. Geibel, S. Horn, J. Magn. Magn. Mater. 1990, 90-91, 428.
- [213] H. D. Yang, W. H. Lee, Phys. Rev. B 1991, 43, 3664.
- [214] H. R. Ott, E. Felder, S. Tagaki, A. Schilling, S. Sato, M. Komatsubara, Phil. Mag. B 1992, 65, 1349.
- [215] A. Krimmel, A. Severing, A. Murani, A. Grauel, S. Horn, Physica B 1992, 180-181, 191.
- [216] A. Mielke, E.-W. Scheidt, J. J. Rieger, G. R. Stewart, Phys. Rev. B 1993, 48, 13985.
- [217] A. Mielke, R. Kolb, J. J. Rieger, E.-W. Scheidt, G. R. Stewart, Physica B 1995, 206-207, 323.
- [218] E.-W. Scheidt, D. Maurer, A. Weber, T. Götzfried, K. Heuser, S. Kehrein, R. Tidecks, Physica B 2002, 321, 133.
- [219] A. M. Strydom, J. L. Snyman, D. Britz, Phys. Stat. Sol. B 2013, 250, 626,
- [220] O. Isnard, S. Miraglia, R. Welter, B. Malaman, J. Synchrotron Rad. 1999, 6, 701.
- [221] R. Sarkar, M. Baenitz, J. Sereni, C. Geibel, J. Phys.: Conf. Ser. 2010, 200, 012173.
- [222] Y. Oner, O. Kamer, J. H. Ross Jr., C. S. Lue, Y. K. Kuo, Solid State Commun. 2005, 136, 533.
- [223] B. M. Sondezi-Mhlungu, D. T. Adroja, A. M. Strydom, W. Kockelmann, E. A. Goremychkin, J. Phys.: Conf. Ser. 2010, 200, 012190.
- [224] B. J. Gibson, R. Pöttgen, R. K. Kremer, Physica B 2000, 276-278, 734.
- [225] B. J. Gibson, W. Schnelle, R. Pöttgen, K. Bartkowski, R. K. Kremer, Cz. J. Phys. 1996, 46 (Suppl. S5), 2573.

- [226] J. Sakurai, K. Kegai, K. Nishimura, Y. Ishikawa, K. Mori, Physica B 1993, 186-188, 583.
- [227] H. Nakotte, E. Brück, K. Prokes, J. H. V. J. Brabers, F. R. de Boer, L. Havela, K. H. J. Buschow, Y. Fu-Ming, J. Alloys Compd. 1994, 207/208, 245.
- [228] G. M. Kalvius, A. Kratzer, H. Nakotte, D. R. Noakes, C. E. Stronach, R. Wäppling, Physica B 2000, 289-290, 252.
- [229] D. R. Noakes, G. M. Kalvius, H. Nakotte, E. Schreier, R. Wäppling, *Physica B* **2002**, *312–313*, 292.
- [230] D. T. Adroja, B. D. Rainford, A. J. Neville, J. Phys.: Condens. Matter 1997, 9, L391.
- [231] S. Baran, J. Leciejewicz, N. Stüsser, A. Szytuła, A. Zygmunt, Y. Ding, J. Magn. Magn. Mater. 1997, 170, 143.
- [232] D. Fus, V. Ivanov, A. Jezierski, B. Penc, A. Szytuła, Acta Phys. Polon, A 2000, 98, 571.
- [233] J. Gegner, H. Wu, K. Berggold, C. P. Sebastian, T. Harmening, R. Pöttgen, L. H. Tjeng, Phys. Rev. B 2008, 77, 035103.
- [234] I. Karla, J. Pierre, A. P. Murani, M. Neumann, *Physica B* **1999**, 271, 294.
- [235] A. Ślebarski, E. D. Bauer, S. Li, M. B. Maple, A. Jezierski, Phys. Rev. B 2001, 63, 125126.
- [236] S. Doniach, Physica 1977, 91B, 231.
- [237] J. R. Iglesias, C. Lacroix, B. Coqblin, Phys. Rev. B 1997, 56, 11820.
- [238] Y.-F. Yang, Z. Fisk, H.-O. Lee, J. D. Thompson, D. Pines, Nature 2008, 454, 611.
- [239] T. Iwasaki, A. Sekiyama, S. Ueda, K. Matsuda, M. Kotsugi, S. Imada, S. Suga, Y. Saitoh, T. Matsushita, T. Nakatani, R. Takayama, O. Sakai, H. Osaka, Kasaya, K. Takegahara, H. Harima, Physica B 2000, 281-282, 105.
- [240] R. Settai, D. Aoki, P. Wiśniewski, Y. Yoshida, A. Mukai, A. Yamaguchi, Y. Ōnuki, S. Yoshii, M. Kasaya, K. Takegahara, H. Harima, Physica B 2000, 281-282, 758.
- [241] K. Katoh, G. Terui, Y. Niide, A. Ochiai, Physica B 2002, 312-313, 239,
- [242] T. Iwasaki, S. Suga, S. Imada, A. Sekiyama, T. Muro, S. Ueda, M. Saeki, H. Harada, T. Matsushita, H. Ishii, O. Sakai, R. Takayama, T. Suzuki, M. Akuura, T. Oguchi, K. Katoh, A. Ochiai, J. Phys. Soc. Jpn. 1999, 68, 1716.
- [243] T. Iwasaki, S. Suga, S. Imada, A. Sekiyama, K. Matsuda, M. Kotsugi, K.-S. An, T. Muro, S. Ueda, T. Matsushita, Y. Saitoh, T. Nakatani, H. Ishii, O. Sakai, R. Takayama, T. Suzuki, T. Oguchi, K. Katoh, A. Ochiai, Phys. Rev. B 2000,
- [244] T. Iwasaki, S. Suga, S. Imada, Y. Kuwata, T. Muro, S. Ueda, M. Saeki, H. Harada, M. Tsunekawa, T. Matsushita, A. Sekiyama, A. Fujimori, H. Ishii, T. Kimura, T. Miyahara, T. Suzuki, K. Katoh, A. Ochiai, J. Electr. Spectr. Rel. Phen. **1998**, 88-91, 309.
- [245] S. Suga, A. Sekiyama, J. Electr. Spectr. Rel. Phen. 2001, 114-116, 659.
- [246] S. Yoshii, H. Suzuki, T. Miyazaki, M. Kasaya, J. Magn. Magn. Mater. 1998, 177-181, 427.
- [247] S. Kimura, K. G. Nath, Y. Haruyama, T. Kinoshita, S. Yoshii, M. Kasaya, Physica B 1999, 259-261, 1163.
- [248] S. K. Malik, D. T. Adroja, Phys. Rev. B 1991, 43, 6295.
- [249] O. Trovarelli, J. G. Sereni, G. Schmerber, J. P. Kappler, Phys. Rev. B 1994, 49, 15179.
- [250] B. D. Rainford, D. T. Adroja, J. M. E. Geers, Physica B 1994, 199-200, 556.

- [251] P. C. Riedi, J. G. M. Armitage, J. S. Lord, D. T. Adroja, B. D. Rainford, D. Fort, Physica B 1994, 199-200, 558.
- [252] B. D. Rainford, D. T. Adroja, A. J. Neville, D. Fort, Physica B **1995**, *206–207*, 209.
- [253] M. J. Thornton, J. G. M. Armitage, R. H. Mitchell, P. C. Riedi, D. T. Adroja, B. D. Rainford, D. Fort, *Phys. Rev. B* 1996, 54, 4189.
- [254] J. S. Lord, G. J. Tomka, P. C. Riedi, M. J. Thornton, B. D. Rainford, D. T. Adroja, D. Fort, J. Phys.: Condens. Matter **1996**. 8. 5475.
- [255] A. J. Neville, B. D. Rainford, D. T. Adroja, H. Schober, Physica B **1996**, *223–224*, 271.
- [256] P. C. Riedi, M. J. Thornton, J. G. M. Armitage, J. S. Lord, G. J. Tomka, D. Fort, Physica B 1997, 230-232, 217.
- [257] A. L. Cornelius, A. K. Gangopadhyay, J. S. Schilling, W. Assmus, Phys. Rev. B 1997, 55, 14109.
- [258] Y. Bando, T. Suemitsu, K. Takagi, H. Tokushima, Y. Echizen, K. Katoh, K. Uemo, Y. Maeda, T. Takabatake, J. Alloys Compd. 2000, 313, 1.
- [259] A. Ślebarski, J. Alloys Compd. 2006, 423, 15.
- [260] M. Kasaya, H. Suzuki, T. Yamaguchi, K. Katoh, J. Phys. Soc. Jpn. 1992, 61, 4187.
- [261] M. Kasaya, H. Suzuki, K. Katoh, M. Inoue, T. Yamaguchi, JJAP Series 1993, 8, 223.
- [262] K. H. Kim, M. H. Jung, Y. S. Kwon, H. Suzuki, M. Kasaya, K. Katoh, T. Takabatake, Physica B 1997, 230-232, 155.
- [263] F. M. Schappacher, P. Khuntia, A. K. Rajarajan, M. Baenitz, J. A. Mydosh, B. Chevalier, S. F. Matar, R. Pöttgen, Z. Naturforsch. 2012, 67b, 473.
- [264] R. Pöttgen, Z. Naturforsch. 2006, 61b, 677.
- [265] K. Łątka, R. Kmieć, J. Gurgul, J. Alloys Compd. 2001, 319, 43.
- [266] K. Łątka, W. Chajec, K. Kmieć, A. W. J. Pacyna, J. Magn. Magn. Mater. 2001, 224, 241.
- [267] R. Pöttgen, D. Johrendt, Z. Naturforsch. 2008, 63b, 1135.
- [268] B. Chevalier, S. F. Matar, M. Ménétrier, J. Sanchez Marcos, J. Rodriguez Fernandez, J. Phys.: Condens. Matter 2006, 18, 6045.
- [269] C. Krellner, N. S. Krini, E. M. Brüning, K. Koch, H. Rosner, M. Nicklas, M. Baenitz, C. Geibel, Phys. Rev. B 2007, 76, 104418.
- [270] J. Rodríguez Fernández, D. P. Rojas, J. C. Gómez Sal, S. Tencé, B. Chevalier, J. Phys.: Conf. Ser. 2010, 200, 012167.
- [271] S. Tencé, G. André, E. Gaudin, B. Chevalier, J. Phys.: Condens. Matter 2008, 20, 255239.
- [272] S. F. Matar, Phys. Rev. B 2007, 75, 104422.
- [273] M. Pasturel, J.-L. Bobet, F. Weill, B. Chevalier, J. Alloys Compd. 2004, 383, 118.

- [274] T. I. Ivanova, I. G. Makhro, M. B. Minko, S. A. Nikitin, Yu. F. Popov, O. D. Chistyakov, Fiz. Met. Metallov. 1993, 76, 134.
- [275] S. A. Nikitin, O. V. Nekrasova, T. I. Ivanova, Yu. F. Popov, Vestn. Mosk. Univ., Ser. 3: Fiz., Astr. 1992, 33, 101.
- [276] J. G. Sereni, M. G. Berisso, N. C. Canales, M. Deppe, C. Geibel, Phys. Stat. Sol. B 2010, 247, 707.
- [277] O. Niehaus, U. Ch. Rodewald, P. M. Abdala, R. S. Touzani, B. P. T. Fokwa, O. Janka, Inorg. Chem. 2014, 53, 2471.
- [278] B. C. Sales, D. K. Wohlleben, Phys. Rev. Lett. 1975, 35, 1240.
- [279] A. Ślebarski, W. Głogowski, J. Goraus, D. Kaczorowski, Phys. Rev. B 2008, 77, 125135.
- [280] W. H. Lee, H. C. Ku, R. N. Shelton, Phys. Rev. B 1987, 36, 5739.
- [281] R. Kolb, A. Mielke, E.-W. Scheidt, G. R. Stewart, J. Alloys Compd. 1996, 239, 124.
- [282] D. E. Barnes, R. N. Shelton, Physica C 1991, 185-189, 2647.
- [283] Y.-W. Shang, H.-H. Sung, W.-H. Lee, Jpn. J. Appl. Phys. 2004, 43, L1346.
- [284] S. C. Chen, J. R. Lee, K. J. Syu, W. H. Lee, Solid State Commun. 2014, 195, 6.
- [285] O. Niehaus, B. Chevalier, P. M. Abdala, F. Winter, R. Pöttgen, Z. Naturforsch. 2013, 68b, 1279.
- [286] O. Niehaus, P. M. Abdala, J. F. Riecken, F. Winter, B. Chevalier, R. Pöttgen, Z. Naturforsch. 2013, 68b, 960.
- [287] O. Niehaus, P. M. Abdala, R. S. Touzani, B. P. T. Fokwa, R. Pöttgen, Solid State Sci. 2015, 40, 36.
- [288] O. Niehaus, P. M. Abdala, R. Pöttgen, Z. Naturforsch. 2015, 70b, 253.
- [289] A. Ślebarski, W. Głogowski, A. Jezierski, J. Deniszcyk, A. Czopnik, A. Zygmunt, Phys. Rev. B 2004, 70, 184429.
- [290] D. T. Adroja, J. G. M. Armitage, P. C. Riedi, M. R. Lees, O. A. Petrenko, Phys. Rev. B 2000, 61, 1232.
- [291] A. Ślebarski, M. Radłowska, A. Zygmunt, A. Jezierski, Phys. Rev. B 2002, 65, 205110.
- [292] L. Menon, S. K. Malik, Phys. Rev. B 1997, 55, 14100.
- [293] B.-L. Young, D. E. MacLaughlin, M. S. Rose, K. Ishida, O. O. Bernal, H. G. Lukefahr, K. Heuser, G. R. Stewart, N. P. Butch, P.-C. Ho, M. B. Maple, Phys. Rev. B 2004, 70, 024401.
- [294] S. Horn, A. Mehner, C. Kämmerer, B. Seidel, C. D. Bredl, C. Geibel, F. Steglich, J. Magn. Magn. Mater. 1992, 108, 205.
- [295] T. Götzfried, A. Weber, K. Heuser, D. Maurer, E.-W. Scheidt, S. Kehrein, G. R. Stewart, J. Low Temp. Phys. 2002, 127, 51.
- [296] B.-L. Young, D. E. MacLaughlin, M. S. Rose, K. Ishida, O. O. Bernal, H. G. Lukefahr, K. Heuser, G. R. Stewart, Phys. Rev. B 2004, 70, 174430.